

Dual Band, Dual Polarization Array Antenna for mm-Wave Radio

Capped Bow-Tie Antenna Elements in a Tightly Coupled Array
Antenna

Master's thesis in Wireless, Photonics and Space Engineering

NIKOLAOS FOKOS

MASTER'S THESIS 2017:NN

Dual Band, Dual Polarization Array Antenna for mm-Wave Radio

Capped Bow-Tie Antenna Elements in a Tightly Coupled Array
Antenna

NIKOLAOS FOKOS



CHALMERS
UNIVERSITY OF TECHNOLOGY

Department of Signals and Systems
Division of Antenna Systems
CHALMERS UNIVERSITY OF TECHNOLOGY
Gothenburg, Sweden 2017

Dual Band, Dual Polarization Array Antenna for mm-Wave Radio
Capped Bow-Tie Antenna Elements in a Tightly Coupled Array Antenna
NIKOLAOS FOKOS

© NIKOLAOS FOKOS, 2017.

Supervisors: Stefan Thöresson, Ericsson AB

Lars Manholm, Ericsson AB

Martin N. Johansson, Ericsson AB

Examiner: Prof. Jian Yang, Department of Signals and Systems

Master's Thesis 2017:NN
Department of Signals and Systems
Division of Antenna Systems
Chalmers University of Technology
SE-412 96 Gothenburg
Telephone +46 31 772 1000

Ericsson AB
SE-417 56 Gothenburg
Telephone +46 10 719 0000

Cover: Capped bow-tie array antenna visualization constructed in HFSS.

Typeset in L^AT_EX
Gothenburg, Sweden 2017

Dual Band, Dual Polarization Array Antenna Element for mm-Wave Radio
Capped Bow-Tie Antenna Elements in a Tightly Coupled Array Antenna
NIKOLAOS FOKOS
Ericsson AB
Department of Signals and Systems
Chalmers University of Technology

Abstract

The combination of a traditional point-to-point (PtP) frequency band and E-band in a single radio unit will increase the spectrum efficiency, the peak capacity, the effective throughput and the service availability for wireless backhaul. The dual polarization capped bow-tie antenna element in a tightly coupled array (TCA) configuration is designed to perform as a dual band (23 GHz band and E-band), dual polarization PtP planar array antenna. The planar array is implemented in printed circuit board (PCB) technology, which is low cost, flexible and provide high mechanical reliability. TCAs have ultra-wideband performance when placed above a ground plane, as well as high scalability, so as they can be tuned for different combinations of dual band operation inside a fractional bandwidth of 4.2:1. The return loss of this design is more than 15 dB in both bands and the polarization orthogonality is more than 27 dB in 23 GHz band, and more than 15 dB in E-band with potential to reach 27 dB. The isolation between horizontal and vertical polarization ports for 23 GHz band is more than 20 dB and from 10 dB to 15 dB for E-band. The return loss of the design displays a shift in frequency in lower band and 2 dB to 6 dB degradation in the higher band with 10% variance of the structure's dimensions, as the element impedance is affected. In addition, a 2-by-1 sub-array is proposed for fabrication and measurement in order to validate the design.

Keywords: Dual band, Dual polarization, E-band, PCB array antennas, TCAs, Wireless backhaul, PtP antennas

Acknowledgements

I would like to express my appreciation to my supervisor Stefan Thöresson and to my manager Daniel Gillén from Ericsson AB for giving me the opportunity to work with this project. A special gratitude I give to my co-supervisors Lars Manholm and Martin N. Johansson for their stimulating suggestions and their guidance to the right path.

Furthermore I would also like to thank Sadegh Mansouri Moghaddam for his help and support during this period. Finally, a special thank you to Prof. Jian Yang not only for being my examiner but also for his continuous encouragement.

Nikolaos Fokos, Gothenburg, June 2017

Abbreviations

balun	Balance to unbalance
GSG	Ground-signal-ground
HOR	Horizontal
LOS	Line-of-sight
NLOS	Non Line-of-sight
PCB	Printed circuit board
PtP	Point-to-point
PtMP	Point-to-multi-point
TCA	Tightly coupled array
UWB	Ultra-wide band
VER	Vertical
VSWR	Voltage standing wave ratio
XPD	Cross-polarization decoupling

Contents

List of Figures	xiii
List of Tables	xvii
1 Introduction	1
1.1 Motivation	1
1.2 Thesis Contribution	2
1.3 Thesis Outline	2
2 Theory	5
2.1 Planar Phased Array Antennas	5
2.1.1 Radiation Fields	6
2.1.2 Grating Lobes	7
2.1.3 Steering Main Lobe	9
2.1.4 Polarization	9
2.1.5 Directivity	10
2.1.6 Array Gain	11
2.2 Tightly Coupled Array Antennas	13
2.3 Balance to Unbalance Feeding Structures	16
2.4 UWB Antenna Research Activities at Chalmers University of Technology	18
3 Design Analysis and Simulated Results	19
3.1 Dual Polarization Capped Bow-Tie TCA	19
3.1.1 Dual Polarization Bow-Tie Element	19
3.1.2 Analysis of Dual Polarization Capped Bow-Tie TCA	20
3.1.3 Feeding Structure	21
3.2 Simulated Results	22
3.2.1 Return Loss and Isolation	24
3.2.1.1 Common-mode Resonance Frequencies Analysis	25
3.2.2 Co-Polarization and Cross-Polarization	27
3.2.3 Radiation Patterns	30
3.3 Beam Steering	31
3.4 Tolerance Analysis	34
3.4.1 Dimension Tolerance Analysis	34
3.4.2 Material Tolerance Analysis	40

4	Measurement and Fabrication Considerations	43
4.1	Transition from Element to Probe Pad	44
4.2	Prototype Simulated Results	46
5	Conclusion	51
5.1	General Conclusions	51
5.2	Future Work Proposal	52
	Bibliography	53

List of Figures

2.1	Rectangular grid with positions of the elements of the planar array.	6
2.2	(a) Array factor with main and grating lobes, (b) Total radiation pattern [33].	8
2.3	Gain limitation with line losses at 86 GHz for $e_{rad}e_{grt}e_{pol}e_{ill} = 1$	12
2.4	Gain limitation with line losses at 21 GHz for $e_{rad}e_{grt}e_{pol}e_{ill} = 1$	12
2.5	Gain limitation with line losses at 86 GHz for $e_{rad}e_{grt}e_{pol}e_{ill} = 0.6$	13
2.6	Equivalent circuit for a tightly coupled array in free space [27].	14
2.7	(Top) Equivalent circuit for an array in free space. (Bottom) Equivalent circuit for an array with a ground plane [27].	15
2.8	Marchand balun diagram.	16
2.9	(a) Equivalent circuit of a differential feeding network [18]. (b) Lumped impedance equivalent circuit [22]	17
3.1	Progress of dual polarization capped bow-tie element. In the 2-by-1 sub-arrays that are shown the caps (hexagonal copper structures) have been removed from figure for better view of the element, as well as the feeding parts. (a) First design, (b) Slotted element, (c) Slotted and shaped element, (d) Slotted element with extra design freedom.	20
3.2	(a) Multi-layer PCB design of a 4-by-4 sub-array. (b) Substrate design parameters, feeding network included.	21
3.3	(a) Feeding network top view [18]. (b) Twin parallel wire.	22
3.4	Design parameters of dual polarization capped bow-tie. (a) Element, (b) Parasitic Cap, (c) Cap, (d) Feeding Stub.	23
3.5	Return loss simulation result for the infinite array in HFSS software.	24
3.6	Isolation between <i>HOR</i> and <i>VER</i> ports for the infinite array in HFSS software.	25
3.7	Distance between adjacent feeding via holes that cause common-mode resonant frequencies.	26
3.8	Isolation between <i>HOR</i> and <i>VER</i> ports for different values of via hole diameter.	27
3.9	Polarization Parallelity in dB using the Eq. 2.16. Provides the level of orthogonality between the E-field when <i>HOR</i> port is excited and the E-field when <i>VER</i> port is excited.	28
3.10	Cross-polarization Decoupling (XPD) in dB versus frequency when the <i>HOR</i> port is excited, for broadside radiation (8-by-8 elements of the infinite array are excited).	28

3.11	XPD and Polarization Orthogonality in dB versus frequency for broadside radiation (8-by-8 elements of the infinite array are excited).	29
3.12	Normalized 2D radiation pattern at 23 GHz when 8-by-8 elements of the infinite array are excited in HFSS software.	30
3.13	Normalized 2D radiation pattern at 73 GHz when 8-by-8 elements of the infinite array are excited in HFSS software.	30
3.14	Normalized 2D radiation pattern at 83 GHz when 8-by-8 elements of the infinite array are excited in HFSS software.	31
3.15	Planar array located in zy -plane with broadside radiation at \hat{x} direction. E-field vector's direction is the one used for the simulations when VER port is excited.	31
3.16	Return loss for beam steering in the xz -plane of the infinite array in HFSS software.	32
3.17	Realized gain at 22 GHz and 83 GHz for different beam θ angles and $\phi = 0^0$ (in the xz -plane) when 8-by-8 elements of the infinite array are excited in HFSS software.	33
3.18	Return loss for beam steering in the xy -plane of the infinite array in HFSS software.	33
3.19	Realized gain at 22 GHz and 83 GHz for different beam ϕ angles and $\theta = 90^0$ (in the xy -plane) when 8-by-8 elements of the infinite array are excited in HFSS software.	34
3.20	Structure's reflection coefficient variation at 22 GHz for conductor and substrate thickness variation. Simulations made in HFSS.	35
3.21	Structure's reflection coefficient variation at 73 GHz for conductor and substrate thickness variation. Simulations made in HFSS.	35
3.22	Structure's reflection coefficient variation at 83 GHz for conductor and substrate thickness variation. Simulations made in HFSS.	36
3.23	Structure's reflection coefficient variation at 22 GHz for feeding network dimensions variation. Simulations made in HFSS.	36
3.24	Structure's reflection coefficient variation at 73 GHz for feeding network dimension variation. Simulations made in HFSS.	37
3.25	Structure's reflection coefficient variation at 83 GHz for feeding network dimensions variation. Simulations made in HFSS.	37
3.26	Structure's reflection coefficient variation at 22 GHz for element and cap dimensions variation. Simulations made in HFSS.	38
3.27	Structure's reflection coefficient variation at 73 GHz for element dimensions variation. Simulations made in HFSS.	39
3.28	Structure's reflection coefficient variation at 83 GHz for element dimensions variation. Simulations made in HFSS.	40
3.29	Structure's reflection coefficient variation at 22 GHz for material permittivity variation. Simulations made in HFSS.	41
3.30	Structure's reflection coefficient variation at 73 GHz for material permittivity variation. Simulations made in HFSS.	41
3.31	Structure's reflection coefficient variation at 83 GHz for material permittivity variation. Simulations made in HFSS.	41

4.1	2-by-1 dual polarization capped bow-tie sub-array prototype design.	43
4.2	Transition from probe pad to element feeding via hole.	44
4.3	Transmission and reflection coefficients of the transition structure seen in Fig. 4.2.	46
4.4	Return Loss of the two excited horizontal ports. A sub-array of 6- by-7 dual polarization capped bow-tie elements, where only 2-by-1 elements are excited.	47
4.5	Return Loss of the two excited horizontal ports. A sub-array of 3- by-4 dual polarization capped bow-tie elements, where only 2-by-1 elements are excited.	48
4.6	Mutual coupling between horizontal ports. A sub-array of 6-by-7 dual polarization capped bow-tie elements, where only 2-by-1 elements are excited.	48
4.7	Mutual coupling between the first horizontal port and the two vertical non-excited ports. A sub-array of 6-by-7 dual polarization capped bow-tie elements, where only 2-by-1 elements are excited.	49

List of Tables

1.1	Specifications for class 3 antennas at PtP fixed radio systems [37]. . .	2
3.1	Laminate and bonding material properties.	21
3.2	Optimized element design parameter values.	23
3.3	Common-mode resonant frequencies from adjacent feeding via holes. .	26
4.1	Optimized design parameter values for transition from probe pad to element feeding via hole.	45

1

Introduction

1.1 Motivation

Wireless backhaul is the intermediate wireless communication infrastructure for connection between the smaller networks and the primary network, and it is of great importance for mobile network performance. As demands regarding mobile broadband performance are growing, new methods for higher spectrum efficiency are needed.

One of the methods is the Multiband Booster for backhaul, which is the Radio-link bonding (aggregation of carriers into a single virtual one) in different frequency bands, in order to achieve enhanced peak capacity, as well as higher effective throughput if statistical multiplexing is implemented. A bond between a wide high frequency channel and a narrower low frequency one, will significantly improve the service availability and guarantee higher capacity. When the high frequency signal will be degraded due to propagation effects, such as rain, the low frequency will secure the availability. Two potential band combinations are the bond between 18-42 GHz bands and E-band (70/80 GHz) for up to 5 km hops, and the bond between 6-15 GHz bands and 8-48 GHz bands for longer hop distances [30].

In future heterogeneous networks, small cell layers will assist in handling traffic growth. Part of small cells, unable to access the wired backhaul, will be placed between street level and rooftop, and might neither have a clear line-of-sight (LOS) path to a macro site with backhaul. As the use of passive reflectors and repeaters to overcome this problem increases the cost, non line-of-sight (NLOS) backhaul may be the solution. A research carried out by Ericsson showed how point-to-point (PtP) and point-to-multipoint (PtMP) microwave in licensed spectrum could be used for small cell NLOS backhaul [32].

Subsequently, there is great need to develop scalable solutions that will be able to adapt to technology evolution and needs, and at the same time provide lower cost for manufacturing and implementation. In terms of antennas, one proposed solution is to use ultra-wideband dual polarization array antenna optimized to perform at two different frequency bands, that will be used in a single radio unit.

1.2 Thesis Contribution

The aim of this thesis is to investigate the capability of the capped bow-tie antenna element in a tightly coupled array configuration to operate as a dual band and dual polarization planar array antenna for 23 GHz band (21.2-23.6 GHz) and E-band (71-76 & 81-86 GHz). The investigation is localized in PtP antennas for microwave backhaul systems and as a result, the standards of antennas for PtP fixed radio systems from 3 GHz to 60 GHz and for higher frequencies, provided by European Telecommunication Standards Institute (ETSI) [37], [38], constitute the specifications for this work, and are summarized in the Table 1.1. The useful conclusions will be also related to antennas for other type of radio systems.

Table 1.1: Specifications for class 3 antennas at PtP fixed radio systems [37].

Specification	Value	Specification	Value
Gain ¹	32 dBi and 38 dBi	VSWR	< 1.2
Inter-port Isolation	> 35 dB	XPD ²	27 dB

The specification for voltage standing wave ratio is translated to a return loss > 20 dB, however the internal interface requirement for return loss is 15 dB and more.

For single polarization antennas the cross-polarization decoupling (XPD) should be more than 27 dB and for dual polarization antennas the orthogonality between orthogonal ports should be more than 27 dB.

Moreover, in order to test the gain specification a full feeding network for a large array (thousands of elements) must be designed and the losses should be included. This is outside of the scope of this work, and only the approach for calculating the gain versus the size of the array will be shown.

Finally, a proposal for fabrication and measurement of a dual polarization 2-by-1 sub-array prototype is included, in order to validate the design in a future work.

1.3 Thesis Outline

The thesis starts with a description of some fundamental principles of phased array antenna theory, the analysis of the balanced structures, as well as an approach to tightly coupled array theory found in research articles. Chapter 3 contains the detailed design description together with the results taken from HFSS software,

¹Minimum gain for 23 GHz band is 23 dBi and for E-band is 38 dBi [38].

²XPD is the difference in dB between the co-polarized main beam gain and the cross-polarized signal within a defined region [37]. It can be seen as cross-polar decoupling [33].

as well as some problems and some solutions to meet the specifications. Chapter 3 concludes with the dimension tolerance analysis of the structure. The prototype proposal and description is mentioned in Chapter 4. Finally, in Chapter 5 the reader can find the conclusion of this thesis and some suggestions for future work.

2

Theory

In the following sections, the phased array antenna theory is shown, focusing on the principles that are important for this work. It is advised that the reader should look for the entire theory in [33] and [34], as the intention of this work is not to give all the meanings and the important derivations around antenna theory, but only to show the ones behind the simulations that carried out.

2.1 Planar Phased Array Antennas

An array is a collection of elements integrated within one module that includes a signal distribution network. In planar arrays the elements are located in a planar 2D grid in an optimal way to achieve enhanced performance compared to single element antennas. One of main advantages of the array configuration is the possibility of beam shaping, having narrower beam-width that provides higher gain, transmission in longer distances or lower transmitted power.

Moreover, arrays can also be used for beam scanning or even for transmission with multiple beams, as well as the side lobe position and level can be controlled. On the other hand, the cost may be higher, depending on the design. Design and fabrication of arrays are more complicated, compared to horn and reflector antennas.

The radiation pattern (the shape of the levels of radiation in space) of regular arrays can be determined by the following parameters that must be taken into account during the design process:

- The grid geometry
- The distance between the elements (known as Element Spacing)
- The amplitude and the phase of the excitation of each element

2.1.1 Radiation Fields

According to electromagnetic radiation theory for single elements located in free space, the radiated field at a point \mathbf{r} with distance and direction $\hat{\mathbf{r}} = \mathbf{r}/r$ in the far-field is described by [33]:

$$\mathbf{E}(\mathbf{r}) = \mathbf{G}(\hat{\mathbf{r}})e^{jk r}/r \iff \mathbf{E}(r, \theta, \phi) = \mathbf{G}(\theta, \phi)e^{jk r}/r \quad (2.1)$$

where $\mathbf{G}(\hat{\mathbf{r}})$ is a function of amplitude and phase of the field with direction, and k is the wave number. The far-field (or Fraunhofer) is the region that satisfies $r \geq 2D^2/\lambda$, where D is the largest antenna dimension. In this region the radiated field waves are considered planar and the radiation pattern's shape remains constant with distance.

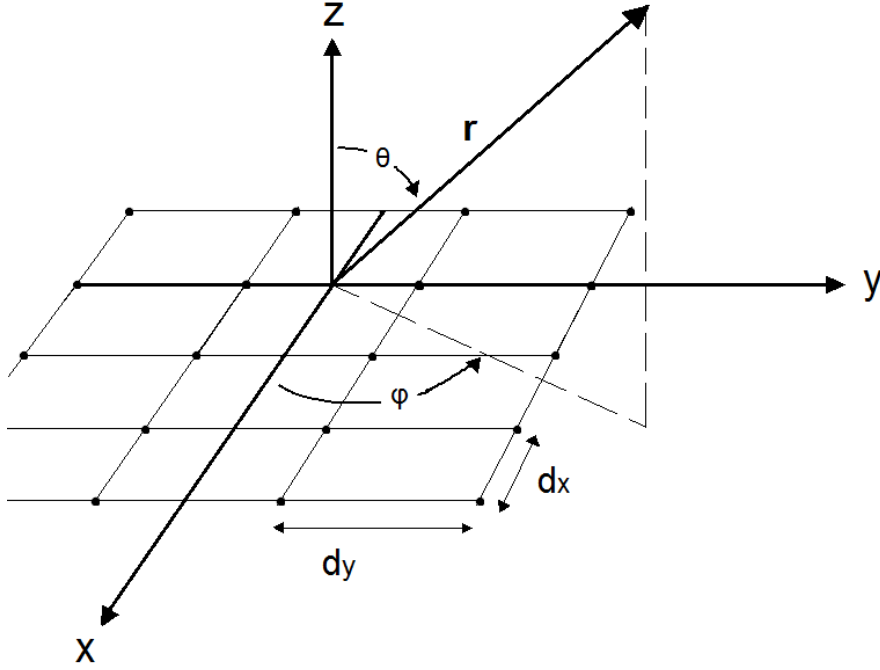


Figure 2.1: Rectangular grid with positions of the elements of the planar array.

For a planar array of equal and equally spaced N by M elements placed in xy - plane as in Fig. 2.1, the radiated field of the nm_{th} element for unit amplitude at a point \mathbf{r} is described as [33]:

$$\mathbf{E}_{nm}(\mathbf{r}) = \frac{1}{r}e^{jk r}\mathbf{G}(\hat{\mathbf{r}})e^{jk\mathbf{R}_{nm}\cdot\hat{\mathbf{r}}} \quad (2.2)$$

where \mathbf{R}_{nm} is the reference point of each element and for $n=1,2,\dots,N$, $m=1,2,\dots,M$ can be written as:

$$\mathbf{R}_{nm} = \mathbf{R}_c + \left(n - \frac{N+1}{2}\right)d_x \hat{\mathbf{x}} + \left(m - \frac{M+1}{2}\right)d_y \hat{\mathbf{y}} \quad (2.3)$$

The geometrical center of the planar array is \mathbf{R}_c and d_x, d_y are the element spacing (distance between adjacent elements) in each direction. The amplitude and the phase of the current excitation of the nm th element are A_{nm} and Φ_{nm} respectively, so after the summation for all the elements the far-field function of the whole array can be written as [33]:

$$\mathbf{G}_A(\hat{\mathbf{r}}) = \sum_{n=1}^N \sum_{m=1}^M A_{nm} e^{j\Phi_{nm}} \mathbf{G}(\hat{\mathbf{r}}) e^{jk\mathbf{R}_{nm} \cdot \hat{\mathbf{r}}} = \mathbf{G}(\hat{\mathbf{r}}) \mathbf{A}\mathbf{F}(\hat{\mathbf{r}}) \quad (2.4)$$

where $\mathbf{G}(\hat{\mathbf{r}})$ is the far-field function of the embedded element and $\mathbf{A}\mathbf{F}(\hat{\mathbf{r}})$ is the array factor [33]:

$$\mathbf{A}\mathbf{F}(\hat{\mathbf{r}}) = \sum_{n=1}^N \sum_{m=1}^M A_{nm} e^{j\Phi_{nm}} e^{jk\mathbf{R}_{nm} \cdot \hat{\mathbf{r}}} \quad (2.5)$$

2.1.2 Grating Lobes

Assuming a smooth and continuous planar phase function of the current excitation:

$$\Phi(x, y) = \Phi_c - k_{\Phi_x} x - k_{\Phi_y} y \quad (2.6)$$

the propagation constants in $\hat{\mathbf{x}}$ and $\hat{\mathbf{y}}$ direction can be written as:

$$\begin{aligned} k_{\Phi_x} &= -\Delta\Phi_x/d_x & \text{with } -\pi < \Delta\Phi_x < \pi \\ k_{\Phi_y} &= -\Delta\Phi_y/d_y & \text{with } -\pi < \Delta\Phi_y < \pi \end{aligned} \quad (2.7)$$

The location of the grating lobes can be found through the maximum values of the array factor:

$$\begin{aligned} K_{xp} &= k_{\Phi_x} + p \frac{2\pi}{d_x}, & p &= \pm 1, \pm 2, \dots, \\ K_{yq} &= k_{\Phi_y} + q \frac{2\pi}{d_y}, & q &= \pm 1, \pm 2, \dots, \end{aligned} \quad (2.8)$$

and if the uv - coordinates are used ($u = \sin \theta \cos \phi$ and $v = \sin \theta \sin \phi$), where $k_x/k = \sin \theta \cos \phi$ and $k_y/k = \sin \theta \sin \phi$, Eq. 2.8 becomes:

$$\begin{aligned}\sin \theta_{pq} \cos \phi_{pq} &= \sin \theta_0 \cos \phi_0 + p \frac{\lambda}{d_x} \\ \sin \theta_{pq} \sin \phi_{pq} &= \sin \theta_0 \sin \phi_0 + q \frac{\lambda}{d_y}\end{aligned}\tag{2.9}$$

The location of the grating lobes can be represented in a rectangular grid in uv -plane, as seen in Fig. 2.2 (a). The total radiation pattern that includes both the main lobe and the grating lobes, is determined by the visible space, which is defined as the area that satisfies $|\sin \theta| \leq 1$ and is represented by the circle in Fig. 2.2 (b).

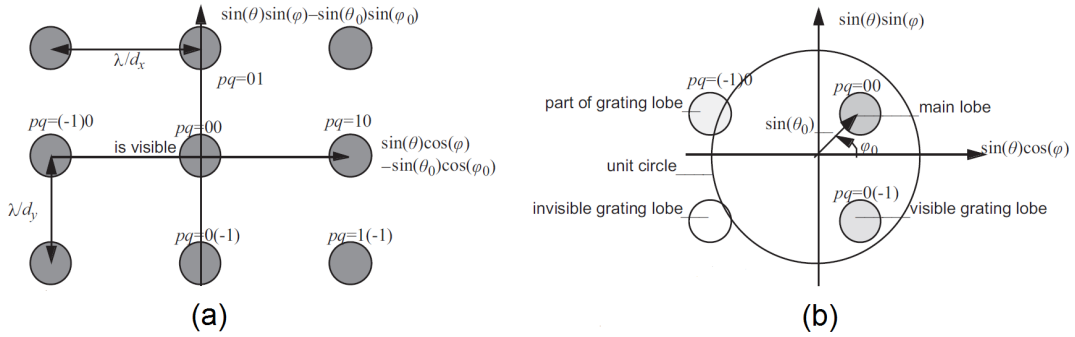


Figure 2.2: (a) Array factor with main and grating lobes, (b) Total radiation pattern [33].

In order to satisfy the requirement for no grating lobes, we can either make sure that they are located outside the visible space, or that they are suppressed by the element pattern. The former is achieved when $\sin \theta_{pq} > 1 + \lambda/D$ for all pq , where D is the diameter of the array in the ϕ -plane, which corresponds to:

$$\sqrt{\left(\sin \theta_0 \cos \phi_0 + p \frac{\lambda}{d_x} + \sin \theta_0 \sin \phi_0 + q \frac{\lambda}{d_y}\right)^2} > 1 + \frac{\lambda}{D}\tag{2.10}$$

Therefore, for broadside transmission (at \hat{z} direction for $\theta, \phi = 0$ according to Fig. 2.2) the sufficient condition for non-radiating grating lobes becomes [33]:

$$\begin{aligned}d_x &\leq \frac{\lambda}{1 + \lambda/D} \\ d_y &\leq \frac{\lambda}{1 + \lambda/D}\end{aligned}\tag{2.11}$$

2.1.3 Steering Main Lobe

An array antenna is able to steer the main beam in a specific direction $\hat{\mathbf{r}}_s = \mathbf{r}_s/r_s$, or (θ_s, ϕ_s) . This can be accomplished by exciting the elements along the vector of steered beam with a linearly progressive phase, while the amplitude is uniform [33]. In this case the array factor becomes:

$$\mathbf{AF}(\hat{\mathbf{r}}) = \sum_{n=1}^N \sum_{m=1}^M A_{nm} e^{j\Phi_{nm}} e^{jk\mathbf{R}_{nm} \cdot \hat{\mathbf{r}}} e^{jk\mathbf{R}_{nm} \cdot \hat{\mathbf{r}}_s} \quad (2.12)$$

When δ_x, δ_y are the phase difference between two adjacent elements in \hat{x}, \hat{y} direction respectively, that are calculated for a specific beam direction, and for

$$\begin{aligned} \xi &= kd_x \cos \phi \sin \theta + \delta_x = kd_x u + \delta_x \\ \eta &= kd_y \sin \phi \sin \theta + \delta_y = kd_y v + \delta_y \end{aligned} \quad (2.13)$$

the array factor becomes:

$$\mathbf{AF} = A_{nm} \sum_{n=1}^N e^{jn\xi} \sum_{m=1}^M e^{jm\eta} \iff |\mathbf{AF}| = \left| \frac{\sin \frac{N\xi}{2}}{N \sin \frac{\xi}{2}} \right| \left| \frac{\sin \frac{M\eta}{2}}{M \sin \frac{\eta}{2}} \right| \quad (2.14)$$

2.1.4 Polarization

The polarization of an electromagnetic wave is determined by the characteristics of the electric field (or E-field). The E-field can have both x - and y - components (assuming propagation at \hat{z} direction), so two different signals at the same frequency can be modulated at the same time in order to double the capacity of the transmission, as long as the fields form a pair of orthogonal polarizations. Orthogonality provides high isolation between the two polarizations as well as low mutual interference. In linear polarization, one component is referred as horizontal (*HOR*) and the other as vertical (*VER*), both relative to the ground. When for example the antenna transmits and receives using the horizontal polarization, the isolation is defined as the ratio between the horizontal and vertical components of E-field. One method to test the isolation is to calculate the *cross-polar decoupling* [33]:

$$(XPD)_{dB} = 10 \log_{10} \left| \frac{E_{co}}{E_{xp}} \right|^2 \quad (2.15)$$

where $\hat{\mathbf{c}}\mathbf{o} = \mathbf{H}\hat{\mathbf{O}}\mathbf{R}$ and $\hat{\mathbf{x}}\mathbf{p} = \mathbf{V}\hat{\mathbf{E}}\mathbf{R}$ for the above example. XPD can also be found as *cross-polar discrimination* and the specification regarding XPD for single polarization PtP antennas is 27 dB [37].

In dual polarization antennas when both polarizations are desirable, one is interested to see how much parallel are the two orthogonal polarizations in terms of E-field vectors. One method to test the orthogonality is to calculate the **Polarization Parallelity**, by exciting both polarizations one at a time, and each time measure the E-field vector in the direction of the excitation. Then the measured E-field vectors are divided by their magnitude to become unit vectors and compared by taking their product:

$$\rho = \frac{\mathbf{E}^{HOR}(\theta, \phi) \cdot \mathbf{E}^{VER}(\theta, \phi)^*}{|\mathbf{E}^{HOR}(\theta, \phi)| |\mathbf{E}^{VER}(\theta, \phi)|} \quad (2.16)$$

where $\mathbf{E}^i = E_{\theta}^i \hat{\boldsymbol{\theta}} + E_{\phi}^i \hat{\boldsymbol{\phi}}$ for $i = HOR$ or VER is the electrical field vector at the far-field when horizontal and when vertical polarization is excited respectively.

In this work the antenna radiates at $\hat{\mathbf{z}}$ direction so in Eq. 2.16 angle θ is zero. When the two polarizations are orthogonal to each other the Eq. 2.16 gives $\rho = 0$, whereas if they are parallel it gives $\rho = 1$. It is convenient to take the logarithm of $1 - \rho$, which is the **Polarization Orthogonality**, and compare it with the level in dB of XPD. We can assume that the specification for polarization parallelity is the same as for XPD (it is not clearly specified from ETSI for dual band antennas).

2.1.5 Directivity

Directivity is defined as the maximum value of the directivity function at the direction of interest. In simple words, it provides an indication of the ability of the antenna to concentrate the beam in a specific direction. So one can use the formula [33]:

$$D = 4\pi \frac{|\mathbf{G}(\theta_0, \phi_0) \mathbf{A}\mathbf{F}(\theta_0, \phi_0) \cdot \hat{\mathbf{c}}\mathbf{o}^*|^2}{P} = e_{grt} e_{pol} e_{ill} \cos \theta_0 D_{max} \quad (2.17)$$

where P is the power integral of the planar array:

$$P = \int_0^{2\pi} \int_0^{2\pi} |\mathbf{G}_A(\theta, \phi)| \sin \theta d\theta d\phi \quad (2.18)$$

where $\mathbf{G}_A(\theta, \phi)$ is the far-field function of the array. The factors in the second part of the equation are the maximum available directivity:

$$D_{max} = \frac{4\pi}{\lambda^2} N A_{cell} \quad \begin{array}{l} N : \text{number of elements} \\ A_{cell} : \text{element aperture area} \end{array} \quad (2.19)$$

the illumination efficiency:

$$e_{ill} = \frac{1}{N A_{cell}} \left| \iint_A A(x, y) d_x d_y \right|^2 / \iint_A |A(x, y)|^2 d_x d_y \quad (2.20)$$

the polarization efficiency:

$$e_{pol} = |\mathbf{G}(\theta_0, \phi_0) \cdot \hat{\mathbf{c}}\mathbf{o}^*|^2 / \left(|\mathbf{G}(\theta_0, \phi_0) \cdot \hat{\mathbf{c}}\mathbf{o}^*|^2 + |\mathbf{G}(\theta_0, \phi_0) \cdot \hat{\mathbf{x}}\mathbf{p}^*|^2 \right) \quad (2.21)$$

and the grating efficiency:

$$e_{grt} = |\mathbf{G}(\theta_0, \phi_0)|^2 / \left(\sum_{pq} |\mathbf{G}(\theta_{pq}, \phi_{pq})|^2 \frac{\cos \theta_0}{\cos \theta_{pq}} \right) \quad (2.22)$$

2.1.6 Array Gain

The realized gain G_{array} of a passive array with equally spaced and equal element size and shape can be found if the second part of the equation 2.17 is multiplied by the radiation efficiency e_{rad} , which is the ratio between the radiated and the incident power. So the realized gain can be expressed as [33]:

$$G_{array} = e_{rad} e_{grt} e_{pol} e_{ill} \cos \theta_0 D_{max} \quad (2.23)$$

In the Eq. 2.23 the array realized gain increases linearly with the number of elements. When the number of elements are small the feeding network losses are not too large, so the gain continues to increase with size. However, the gain is ultimately limited if the losses are not negligible. For a planar array of N elements with element spacing d in both directions and transmission lines with length $(N^{1/2} - 1)d$, the realized gain at broadside when all elements are assumed matched is given by [34]:

$$G_{array} = e_{rad} e_{grt} e_{pol} e_{ill} \frac{4\pi}{\lambda^2} N A_{cell} 10^{-(d/\lambda)(N^{1/2}-1)(a_{dB/\lambda}/10)} \quad (2.24)$$

where $a_{dB/\lambda}$ is the loss of the transmission line in decibels per wavelength due to attenuation, and A_{cell} is the aperture area of a single element. In order to be more precise, the losses due to power divider need to be added for the total losses.

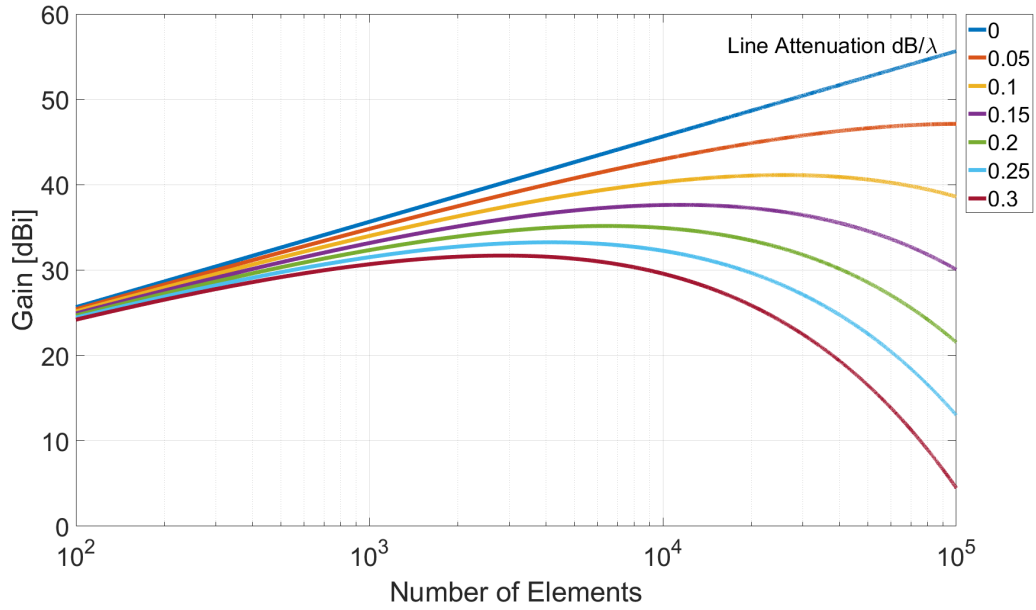


Figure 2.3: Gain limitation with line losses at 86 GHz for $e_{rad}e_{grt}e_{pol}e_{ill} = 1$.

In Fig. 2.3 we can see the gain in dBi versus the number of elements in a planar array for different transmission line losses at 86 GHz. For this scenario it is assumed that illumination, polarization, grating and radiation efficiency are one (ideal case). In addition, the element spacing is 1.894 mm in both directions as this is the value that used in the simulations of this work. It is obvious that the maximum achievable gain saturation depends on the line losses of the feeding network.

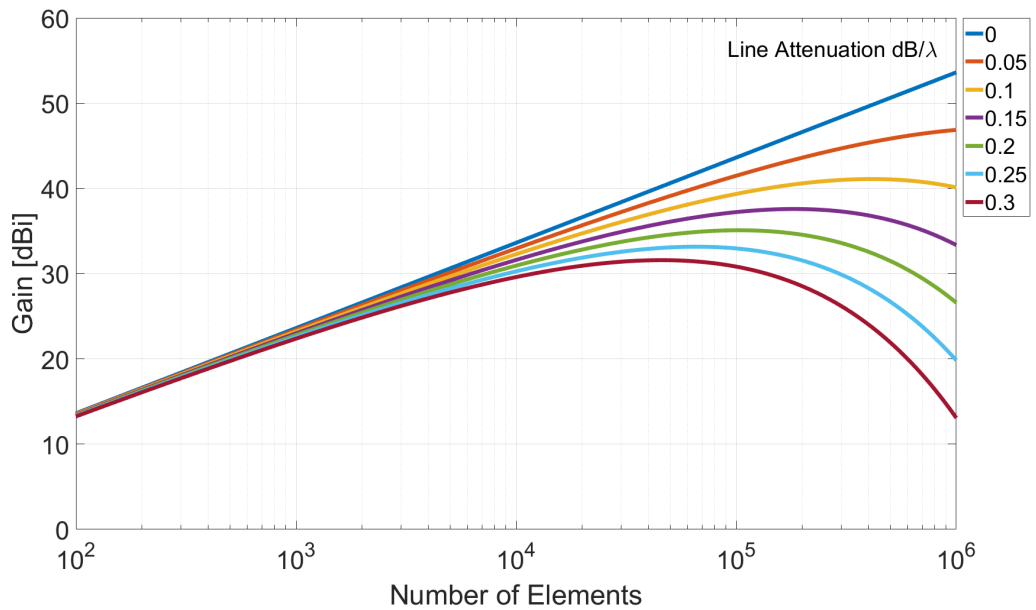


Figure 2.4: Gain limitation with line losses at 21 GHz for $e_{rad}e_{grt}e_{pol}e_{ill} = 1$.

In Fig. 2.4 we can see the gain limitation for 21 GHz under the same assumptions. It is observed that the maximum gain is at the same level as in 86 GHz and with the same element spacing more elements required to achieve that gain.

Finally, in Fig. 2.5 we can see the gain limitation at 86 GHz in a more realistic case where $e_{rad}e_{grt}e_{pol}e_{ill} = 0.6$. The maximum achievable gain saturates faster and is lower in this case, as expected.

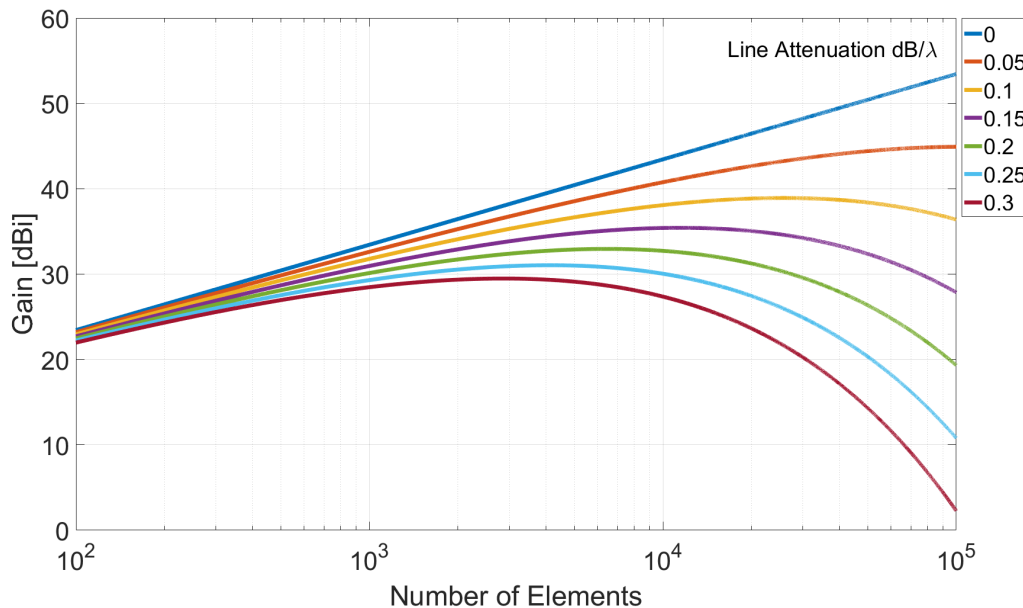


Figure 2.5: Gain limitation with line losses at 86 GHz for $e_{rad}e_{grt}e_{pol}e_{ill} = 0.6$.

For example, a waveguide filled with air has approximately $0.004 \text{ dB}/\lambda$ line losses at 10 GHz and a microstrip line around $0.23 \text{ dB}/\lambda$ line losses (alumina substrate) at the same frequency [35]. So for a passive array with $e_{rad}e_{grt}e_{pol}e_{ill} = 0.6$ and microstrip lines, the maximum achievable gain at 86 GHz is around 31 dBi.

2.2 Tightly Coupled Array Antennas

In phased planar array antennas a single element is designed in an infinite array environment (which can be realized by array periodic boundary conditions) so that the mutual coupling is included in the design. The element is then tuned to achieve the desirable bandwidth, return loss and isolation. The array formulation results in an enhanced performance, mainly in terms of directivity, gain and beam shaping, as discussed in the beginning of the Chapter 2. It has been observed [13] that when the elements are tightly coupled and placed above a ground plane, the array can obtain a ultra-wideband performance. Moreover, this behaviour has been modeled [14] and used in designs that can achieve a 4.5:1 fractional bandwidth.

A representation of the equivalent circuit for a tightly coupled dipole array in free space can be seen in Fig. 2.6. For a single element a RLC network is formed from dipole's self inductance (L_{self}), dipole's self capacitance (C_{self}), the radiation resistance ($R_{rad} = 2R$) and the mutual capacitance (C_{couple}) between elements, with a resonance frequency [27]:

$$f_r = \frac{1}{2\pi\sqrt{2L_{self}(C_{self} + C_{couple})}} \quad (2.25)$$

If the dipoles were connected with infinite capacitance ($C_{couple} = \infty$), which is a short, then the array would be a wire array with very narrowband performance. Therefore, for wideband performance the planar arrays must be capacitively coupled rather than shorted [27].

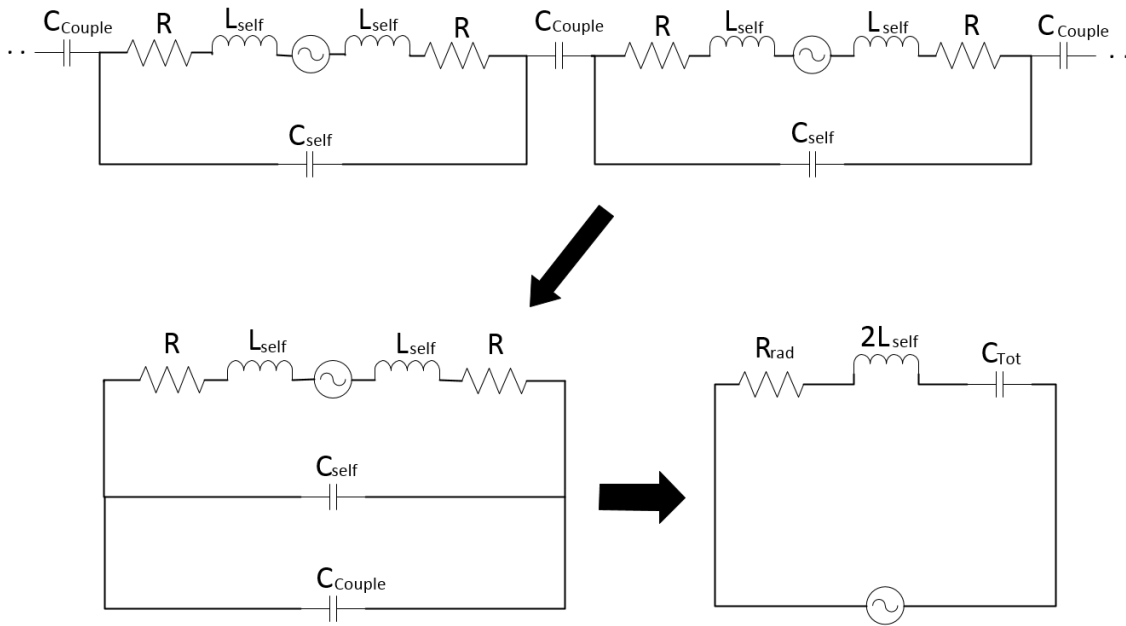


Figure 2.6: Equivalent circuit for a tightly coupled array in free space [27].

At approximately 0.3λ distance from the ground plane (λ is calculated for the highest frequency of interest), the inductive reactance of ground plane and the capacitive reactance of array are cancelled for low frequencies, as well as the capacitive reactance of ground plane and the inductive reactance of array are cancelled for high frequencies, resulting in an antenna with a resistive behaviour that can achieve more than 4:1 fractional bandwidth [28].

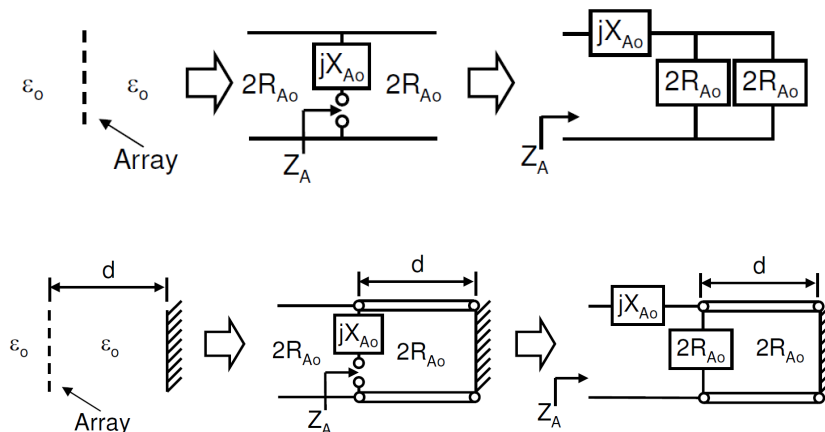


Figure 2.7: (*Top*) Equivalent circuit for an array in free space. (*Bottom*) Equivalent circuit for an array with a ground plane [27].

In order to understand the effect of the ground plane one can refer to equivalent circuit that can be seen in Fig. 2.7. The top sub-figure illustrates the circuit representation of an ideal array in free space, where the elements are electrically small with absence of grating lobes making the circuit valid. Assuming that the two half spaces have characteristic impedance $2R_{A0}$, the input impedance of the array becomes (the symbols are kept the same as the reference article for simplicity) [27]:

$$Z_A = R_{A0} + jX_{A0} \quad (2.26)$$

where X_{A0} is the array reactance. In the bottom sub-figure the ground plane has been inserted, which has an impedance from transmission line theory [35]:

$$Z_{gp} = 2R_{A0}(Z_L + 2R_{A0} \tan\beta d)/(2R_{A0} + Z_L \tan\beta d) \quad (2.27)$$

So the input impedance of the array becomes [27]:

$$Z_A = 2R_{A0}/Z_{gp} + jX_{A0} \quad (2.28)$$

As a result, the Eq. 2.28 obtains two solutions, which can be represented in *Smith Chart* where the curve of Z_A gets a second passage from the center [27].

In conclusion, a good interpretation of the behaviour of this technology can be summarized with the phrase of Moulder et al. [20], “**Tightly coupled arrays (TCAs) act as “meta-structured” apertures rather than arrays of discrete elements**”. Recent work in the field of TCA technology can be found in [14], [17], [18], [19], [20] and [21].

2.3 Balance to Unbalance Feeding Structures

In a “balanced” connection between two circuits or between two devices, the signal is between two terminals - conductors that have the same impedance to ground. In a proper balanced connection, a balanced output must be connected to a differential input, where the two conductors transmit the same signal with opposite polarity.

Many types of antennas, for example dipole or bow-tie antennas, have a differential input and require a transformer before them in order to be connected with a circuit that has a single-ended signal as output. Those transformers, which are called **baluns** (balance-to-unbalance), are very important elements for the performance of the antenna and usually are the limiting factors in terms of bandwidth, losses, space requirements and cost.

It has been an extensive work around the design and implementation of baluns in antenna structures. However, only the analysis of the Marchand BALUN and a version of it [18] will be presented, as they are used to feed the element of this work. The reader can refer to [28] and [29] for more information regarding some different balun designs and their advantages and disadvantages.

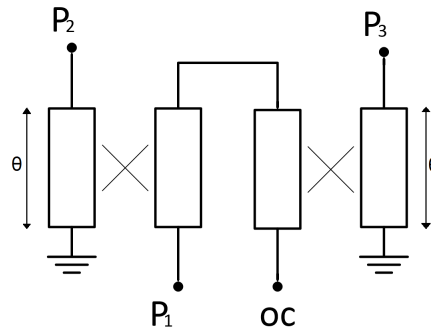


Figure 2.8: Marchand balun diagram.

The diagram of a Marchand balun can be seen in Fig. 2.8. It is based on two coupled line couplers (theory is available at [35]) and the S-parameters can be written as [15] (symbols are kept same as the reference article):

$$\begin{aligned}
 S_{11} &= \frac{x^4 - y^4 - y^2 z^2}{z^2(z^2 + y^2)} & S_{22} = S_{33} &= \frac{-x^2 z^2}{z^2(z^2 + y^2)} \\
 S_{12} = S_{21} &= \frac{x^3 y - x y z^2 - x^3 y}{z^2(z^2 + y^2)} & S_{13} = S_{31} &= \frac{x y z^2 + x y^3 - x^3 y}{z^2(z^2 + y^2)} \\
 S_{23} = S_{32} &= \frac{y^4 + y^2 z^2 - x^2 y^2}{z^2(z^2 + y^2)}
 \end{aligned} \tag{2.29}$$

where $x = \sqrt{1 - k^2}$, $y = jk \sin \theta$ and $z = \sqrt{1 - k^2} \cos \theta + j \sin \theta$, k is the coupling coefficient between the coupled lines and θ is the electrical length [15]. The most important performance characteristics of the balun that should be taken into account during design process are following:

- **Frequency Range**
- **Amplitude & Phase Balance** - How close to equal power and 180° phase difference are the output signals.
- **Common Mode Rejection Ratio** - Total common-mode signal attenuation/rejection.
- **Return Loss** - The ratio of the signal reflected back from a device under test, to the signal inserted to that device.
- **Impedance Ratio** - The ratio of unbalanced impedance to balanced impedance.

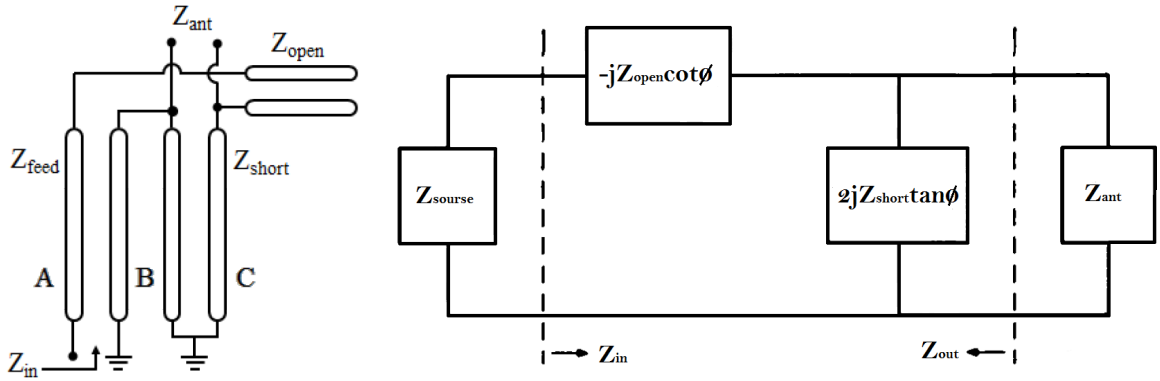


Figure 2.9: (a) Equivalent circuit of a differential feeding network [18]. (b) Lumped impedance equivalent circuit [22].

In Fig. 2.9 (a) there is the equivalent circuit of the differential feeding structure that is used in this work. Markus H. Novak et al. [18] proposed this structure in order to minimize the size and the cost, as it requires three via holes for PCB antenna configuration. It is based on the theory for the optimum design for broadband baluns [22], where the lumped impedance equivalent circuit for such designs can be seen in Fig. 2.9 (b). Using the symbols from [18] the port impedances from [22] can be expressed as:

$$Z_{in} = \frac{4Z_{ant}Z_{short}^2 \tan^2 \theta + j(2Z_{ant}^2 Z_{short} \tan \theta - 4Z_{open}Z_{short}^2 \tan \theta - Z_{ant}^2 Z_{open} \cot \theta)}{4Z_{short}^2 \tan^2 \theta + Z_{ant}^2}$$

$$Z_{out} = \frac{2Z_{short}(2Z_{source}Z_{short} \tan^2 \theta + j(Z_{open}^2 \cot \theta - 2Z_{open}Z_{short} \tan \theta + Z_{source}^2 \tan \theta))}{4Z_{short}^2 \tan^2 \theta + Z_{ant}^2 + Z_{source}^2 \cot^2 \theta - 4Z_{open}Z_{short}}$$
(2.30)

where θ is the electrical length of the *short*-circuit. If the designed balun satisfies the $Z_{short} \gg Z_{open}$ condition then it obtain ultra-wideband (UWB) performance [18].

2.4 UWB Antenna Research Activities at Chalmers University of Technology

The Antenna Group at Chalmers University of Technology has been developing several UWB antennas. Some of the work that has been done and is still carried out is the hat-feed reflector antenna, which is a kind of wideband antenna [1-6] that can be applied in satellite communication systems. The self-grounded bow-tie antenna [7-11] is another kind of UWB antenna and it can be applied under many scenarios, for instance, UWB radar and medical detection. Finally, the quad-ridge horn is an UWB antenna [12] applied mainly in radio telescopes.

3

Design Analysis and Simulated Results

In the following sections, the dual polarization capped bow-tie array antenna design is analyzed and the results from simulations are then discussed.

3.1 Dual Polarization Capped Bow-Tie TCA

3.1.1 Dual Polarization Bow-Tie Element

The design of this work is based on the bow-tie antenna element. In Fig. 3.1 all the versions of the dual polarization element that tested for in this work can be seen.

In the most simple one (*a*), the horizontal and the vertical elements are united. This structure does not have the properties of the tightly coupled arrays, thus provides a fractional bandwidth less than 3:1 when placed above a ground plane. In addition, due to symmetry conservation in horizontal and vertical dimensions, the freedom in design parameters is limited.

Next, the horizontal and vertical elements are separated in Fig. 3.1 (*b*). The slots that are inserted between the elements provide the TCA ultra-wideband property when placed above a ground plane, that together with a parasitic cap on top of the slots, as well as the cap on top of the element, pushes the fractional bandwidth to more than 4:1.

The structure for ideal simulations with lumped ports (does not include a feeding network) revealed that the element differential impedance is around $75\ \text{ohm}$. However, it was observed that when the element is shaped as in Fig. 3.1 (*c*), it obtains differential impedance around $150\ \text{ohm}$ while maintains the same performance. This characteristic gives an extra advantage to the design, as it can be adjusted to operate with different feeding networks, with different manufacturing limitations, that can provide different differential impedance.

Finally, in Fig. 3.1 (d) one extra design parameter is inserted, providing one more freedom for better fine tuning.

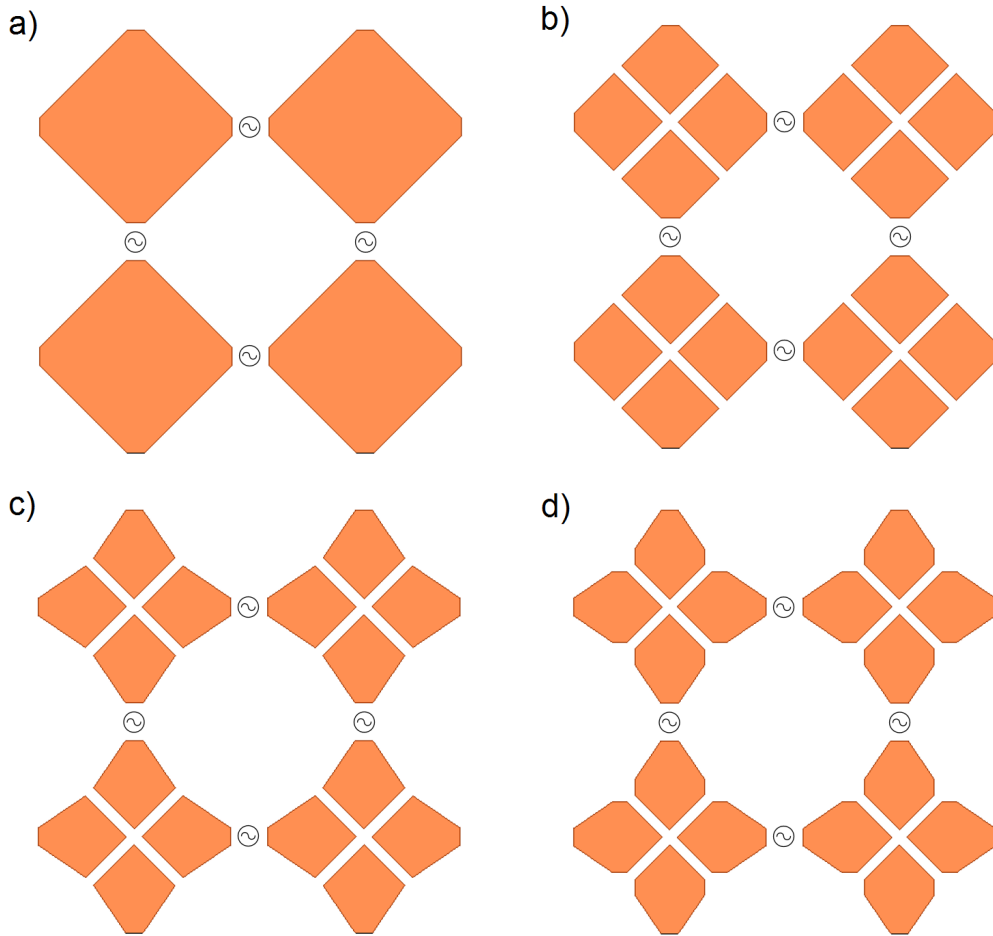


Figure 3.1: Progress of dual polarization capped bow-tie element. In the 2-by-1 sub-arrays that are shown the caps (hexagonal copper structures) have been removed from figure for better view of the element, as well as the feeding parts. (a) First design, (b) Slotted element, (c) Slotted and shaped element, (d) Slotted element with extra design freedom.

3.1.2 Analysis of Dual Polarization Capped Bow-Tie TCA

The dual polarization capped bow-tie array antenna is configured in multi-layer printed circuit board (PCB) technology. Single-layer PCB designs are flexible, their weight is light and they provide high mechanical reliability. On the other hand, the insertion loss is higher compared to horn and parabolic antennas, so achieving high gain is always an issue [36]. Moreover, adding more layers will increase the cost, but still it remains competitive.

In Fig. 3.2 (a) an array antenna structure can be seen. It consists of a core laminate

(the “green” layer) that has the ground plane on the bottom side and the element on the top side. On the top of that, a bonding material follows (the middle “yellow” layer), having the parasitic caps (hexagonal copper structure) and the feeding stubs on top. The properties of the substrates used are summarized in Table 3.1.

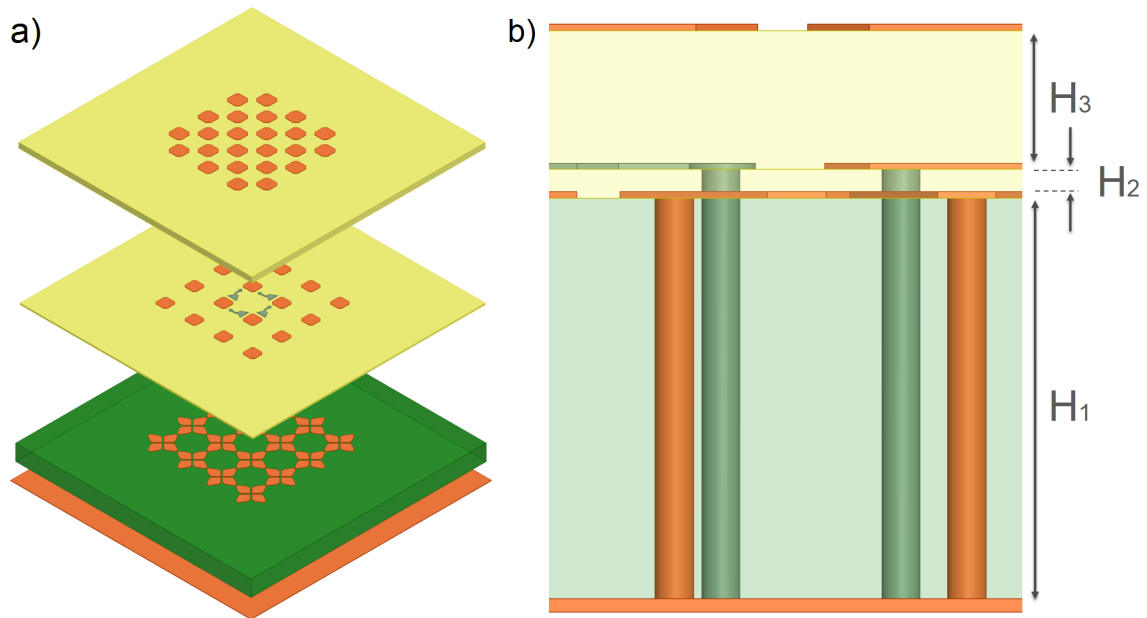


Figure 3.2: (a) Multi-layer PCB design of a 4-by-4 sub-array. (b) Substrate design parameters, feeding network included.

Notice that in this layer only the four feeding stubs are shown. Finally, an extra bonding material follows, which has the caps (hexagonal copper structure) on top. In Fig. 3.2 (b) the side view of the structure can be seen, together with the via holes that are part of the feeding network.

Table 3.1: Laminate and bonding material properties.

Manufacturer	Material	Permittivity	Loss Tangent
Rogers	RT/duriod 5880	2.2	0.0009
Taconic	Fast Rise 27	2.7	0.0014
TUC	TU-933P ¹	3.4	0.0025

3.1.3 Feeding Structure

The feeding structure that is used in this work, is the one that introduced by Novak et al. [18] and its principles were discussed in Chapter 2. The structure consists of three via holes, two that connect each arm with the ground plane and one that

¹TU-933P will be used for measurement purposes that will be seen in Chapter 4

starts from the source below the ground plane and ends in the feeding stub (see Fig. 3.3 (a)). The output differential impedance that is connected to the arms of the bow-tie is considered as the impedance between the two parallel wires (via holes in this case) B and C (see Fig. 3.3 (b)) as seen from the element, and its value can be calculated as [35]:

$$Z_{out} = \sqrt{\frac{\mu}{\epsilon}} \frac{1}{\pi} \operatorname{acosh}\left(\frac{M_1}{\varnothing D}\right) = \frac{120}{\sqrt{\epsilon_r}} \operatorname{acosh}\left(\frac{M_1}{\varnothing D}\right) \quad (3.1)$$

Moreover, it can easily be seen that Z_{short} is the impedance between B and C, Z_{open} is the impedance between the feeding stub and the right arm of the element, Z_{in} is the impedance between A and B as seen from source and its value is determined again by Eq. 3.1. Their relationship is described by Eq. 2.30.

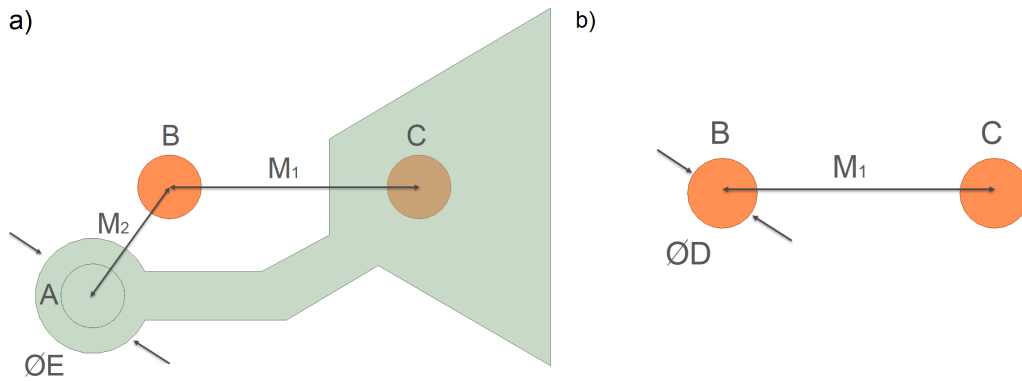


Figure 3.3: (a) Feeding network top view [18]. (b) Twin parallel wire.

It is important to notice that the fabrication limitations regarding the center-to-center distance of via holes when placed in the same layer, as well as the via hole diameter and annular ring, do not allow for Z_{out} to be less than a specific value. This value also depends of the permittivity of the substrate. For a minimum center-to-center distance of via holes 0.3 mm when place in the same layer, minimum via hole diameter 0.1 mm and a material with permittivity 2.2, the differential impedance limitation is around 143 *ohm*.

3.2 Simulated Results

All the simulations of this work are done with HFSS software, provided by **ANSYS**. In order to save simulation time and at the same time take realistic results regarding large array configurations, the infinite array function of the software is used, where a unit cell with element spacing dimensions (S -by- S) is selected and assigned with periodic boundaries (for an array placed in xy - plane that radiates at \hat{z} direction, fields in xz - boundary planes assigned to have the same phase, and so do fields in

yz - boundary planes). Moreover, a floquet port is assigned in xy - plane at the top instead of a radiation boundary. In Fig. 3.4 the capped bow-tie array structure can be seen.

The simulations started with the absence of the balun. A lumped port is used so as to tune the element and achieve the best performance that it could provide in “ideal” situation.

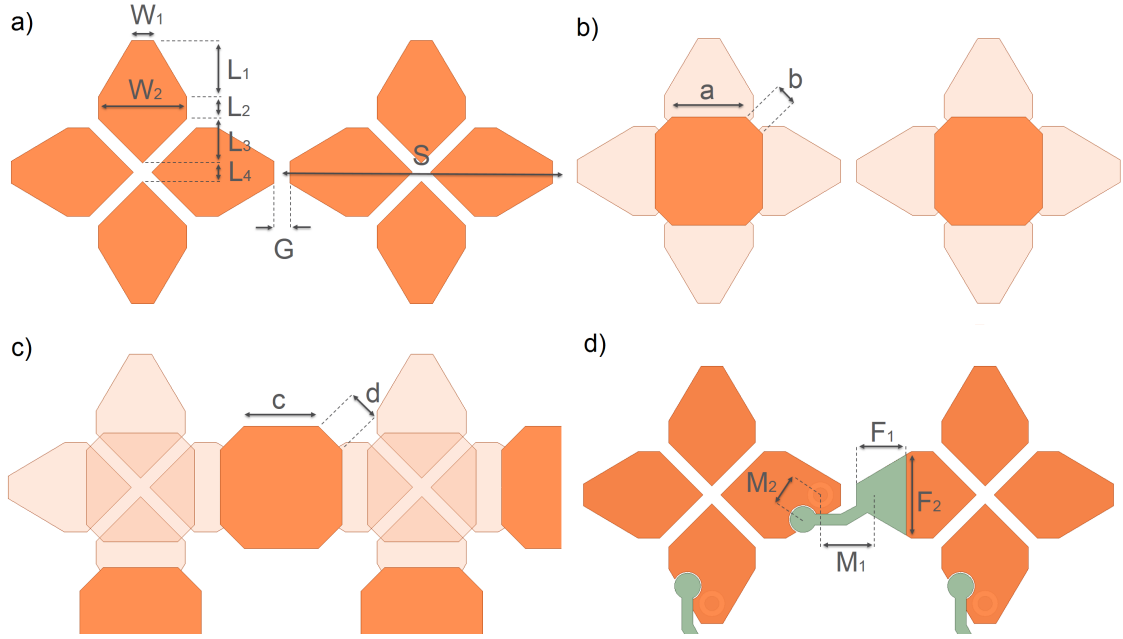


Figure 3.4: Design parameters of dual polarization capped bow-tie. (a) Element, (b) Parasitic Cap, (c) Cap, (d) Feeding Stub.

The balun is added afterwards and the whole structure is tuned again, having the “ideal” situation as the target. In order to visualize the radiation patterns in 23 GHz band, more elements apart from the unit cell needs to be excited for larger aperture area. For that purposed in the infinite array 8-by-8 elements are excited (the array model function is provided by the software). The design parameter values after optimization for best return loss and used for all the figures of this Chapter are summarized in Table 3.2. This work follows the design rules found in [31].

Table 3.2: Optimized element design parameter values.

Parameter	(mm)	Parameter	(mm)	Parameter	(mm)
W_1	0.15	S	1.894	M_1	0.22
W_2	0.6	a	0.5	M_2	0.39
L_1	0.38	b	0.163	H_1	1.03
L_2	0.15	c	0.5	H_2	0.073
L_3	0.3	d	0.226	H_3	0.357
L_4	0.124	F_1	0.346	$\oslash D$	0.1
G	0.11	F_2	0.558	$\oslash E$	0.2

3.2.1 Return Loss and Isolation

The placement of element in xy - plane is symmetric in both directions, whereas the feeding structure is asymmetric. It is tested that there is no difference if the feeding stub is placed in the left or in the right side of the element in a large array. Furthermore, there is no difference which direction is the HOR ports and which the VER ports, as long as they are orthogonal each other. It is assumed that the HOR port is the one seen at the center in Fig. 3.4 (d).

In Fig. 3.5 the return loss of the array when the HOR ports are excited with periodic feeding with zero phase, can be seen. The return loss is >15 dB for both 23 GHz band and E-band, which satisfies the specifications.

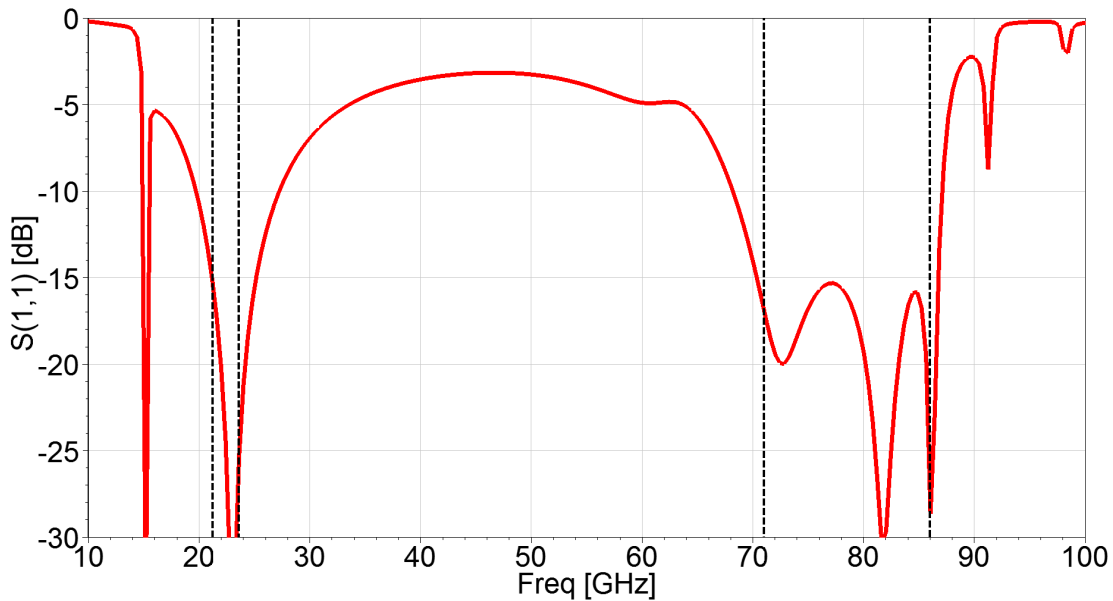


Figure 3.5: Return loss simulation result for the infinite array in HFSS software.

In Fig. 3.6 the isolation between HOR and VER ports of the infinite array, when the HOR ports are excited with periodic feeding with zero phase, can be seen. The isolation in 23 GHz band is better than the isolation in E-band. The decreased isolation is caused by the feeding network, as the feeding via holes for each element are not shielded, having mutual coupling and as a result some resonance frequencies occur close to the frequencies of interest.

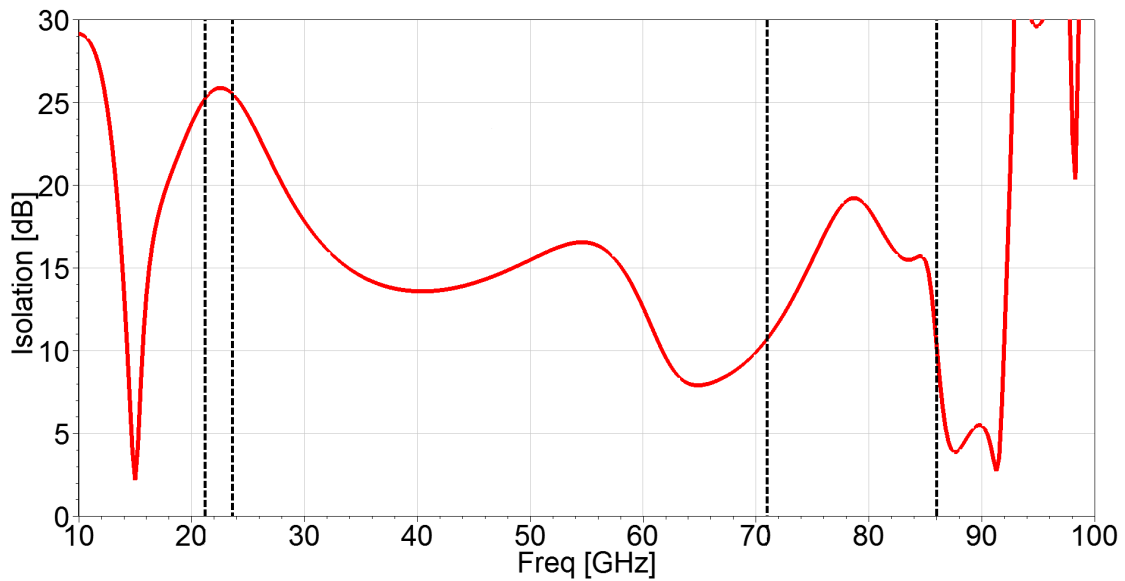


Figure 3.6: Isolation between *HOR* and *VER* ports for the infinite array in HFSS software.

3.2.1.1 Common-mode Resonance Frequencies Analysis

From the isolation plot in Fig. 3.6, one can observe three main peak values of s_{21} dB-curve inside the frequency range, at around 37 GHz, 63 GHz and 88 GHz. This behaviour can be interpreted by the common-mode resonance frequencies that exist due to coupling between the feeding via holes, and can be estimated from [18] using:

$$f_{Resonance} = \frac{C_0}{2D\sqrt{\epsilon_r}} \quad (3.2)$$

where D is the distance between two feeding via holes, C_0 is the speed of light in vacuum and ϵ_r is the relevant permittivity of the material.

If D is replaced by K_1 to N_4 from Fig. 3.7, when ϵ_r is 2.1 (slightly less than 2.2 which is the relevant permittivity of the substrate that is used), the calculated resonance frequencies are summarized in Table 3.3.

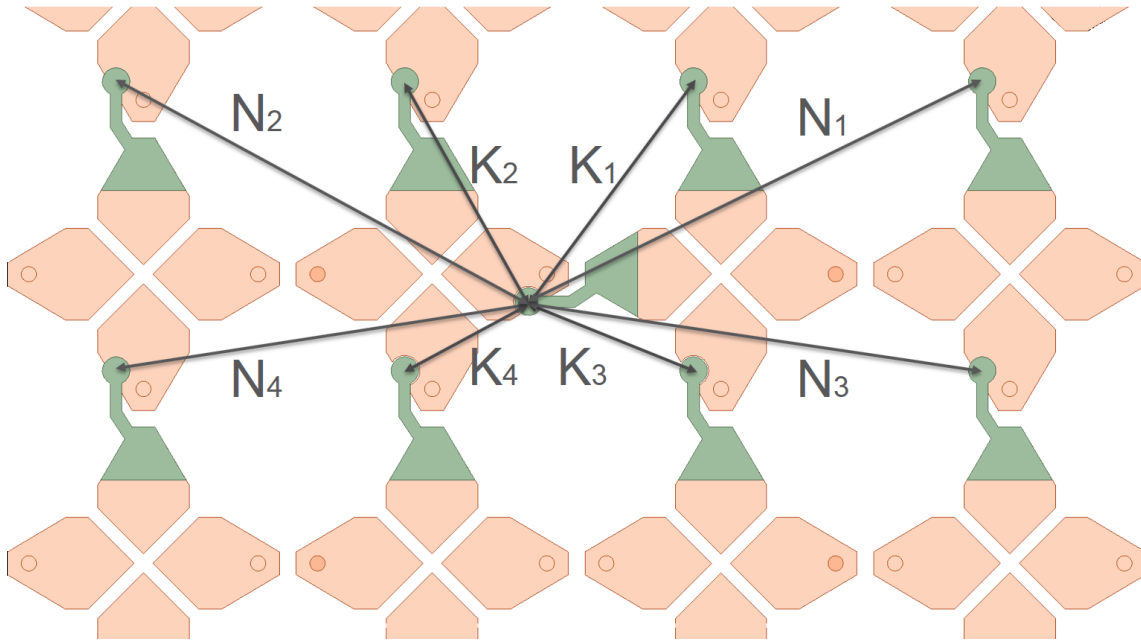


Figure 3.7: Distance between adjacent feeding via holes that cause common-mode resonant frequencies.

The frequencies where the three main peak values of $\text{dB}(S_{21})$ curve (Fig. 3.6) occur, are related to N_1 to N_4 , K_2 and K_3 distances respectively. With careful tuning of the feeding network, the isolation can be improved to a certain level. However, any distance changes that are related to the feeding network affect the output impedance of the structure and as a result the return loss. Therefore, when tuning the feeding network it is necessary to observe isolation and return loss changes at the same time.

Table 3.3: Common-mode resonant frequencies from adjacent feeding via holes.

Parameter	Frequency	Parameter	Frequency
K_1	57.5 GHz	N_1	31.3 GHz
K_2	62.5 GHz	N_2	33.7 GHz
K_3	88.3 GHz	N_3	34.4 GHz
K_4	111.5 GHz	N_4	37.7 GHz

Moreover, there is a relationship between the isolation and the via hole diameter. From Fig. 3.8 it is observed that for thinner via hole the isolation slightly improves at E-band, but becomes worse for 23 GHz band. Again, via hole diameter changes affect the output impedance of the structure and as a consequence the return loss.

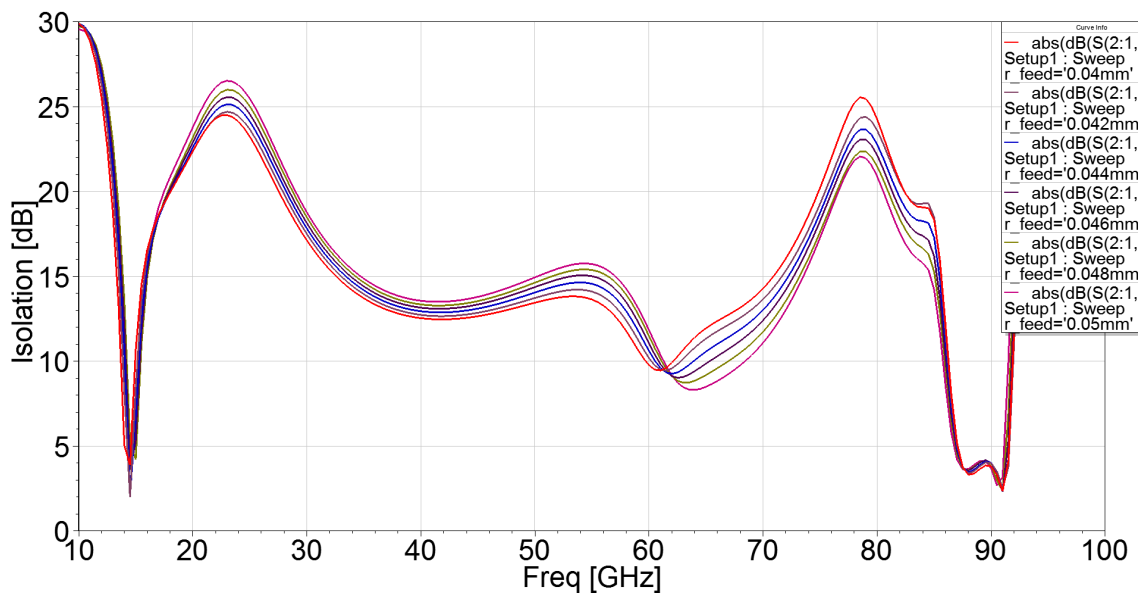


Figure 3.8: Isolation between *HOR* and *VER* ports for different values of via hole diameter.

Another way to improve isolation is to use a feeding network that is shielded with a metal structure so as to avoid radiation. Such an example is the work of Timothy E. Durham et al. [24], which based on the technology developed by D. S. Filipovic et al. [25].

3.2.2 Co-Polarization and Cross-Polarization

In Section 2.1.3 of Chapter 2, the metric Polarization Parallelity and its importance regarding the dual polarization antennas were discussed. In Fig. 3.9 polarization parallelity is plotted versus the frequency for the final design.

For the 23 GHz band the dB level of polarization parallelity is between -38 dB and -60 dB, which fulfills the 27 dB requirement. In addition, from 71 GHz to 76 GHz and from 81 GHz to 84 GHz the polarization parallelity is below -27 dB. However, for 85 GHz and 86 GHz it is below -16 dB, which does not fulfill the requirement. It is clear that there is a strong relationship between the isolation and polarization parallelity. As a result, a more careful tuning of feeding network and element dimensions that will improve isolation at higher frequencies, can also set polarization parallelity to a desirable level.

Polarization parallelity does not provide the information for the direction of E-field vectors, in a sense that E-fields can be orthogonal but might be rotated right/left handed from the original excitation direction, or even have elliptical polarization.

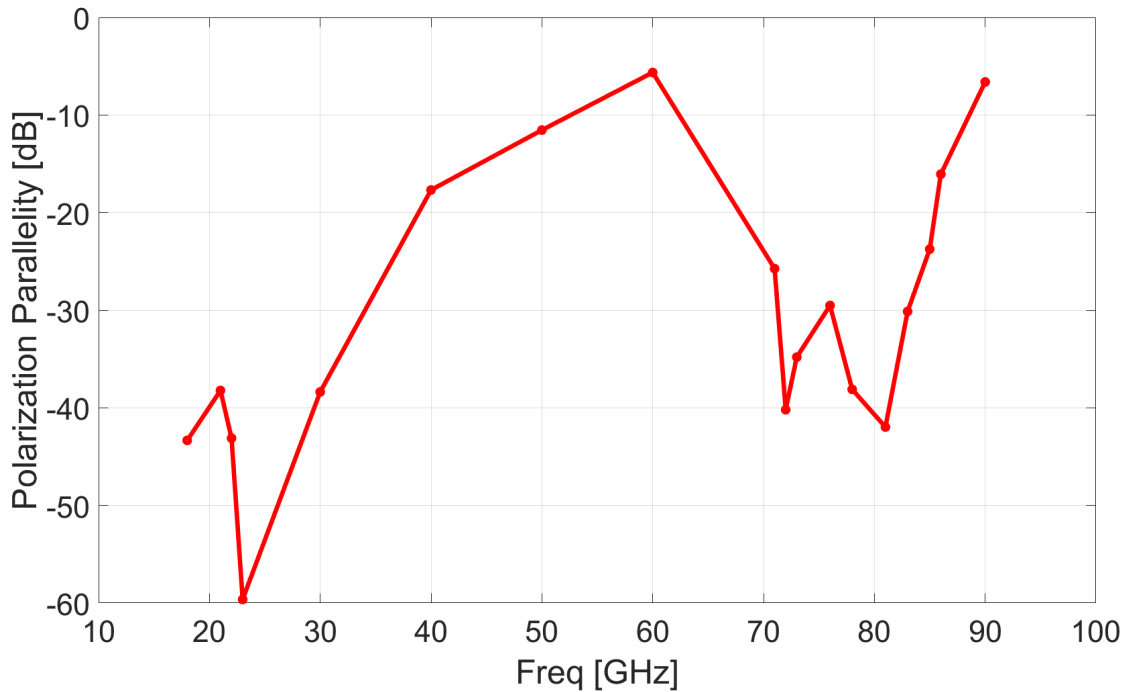


Figure 3.9: Polarization Parallelity in dB using the Eq. 2.16. Provides the level of orthogonality between the E-field when *HOR* port is excited and the E-field when *VER* port is excited.

Through gain simulation in the direction of excitation and in its orthogonal one, XPD is calculated using Eq. 2.15 and it is plotted in Fig. 3.10.

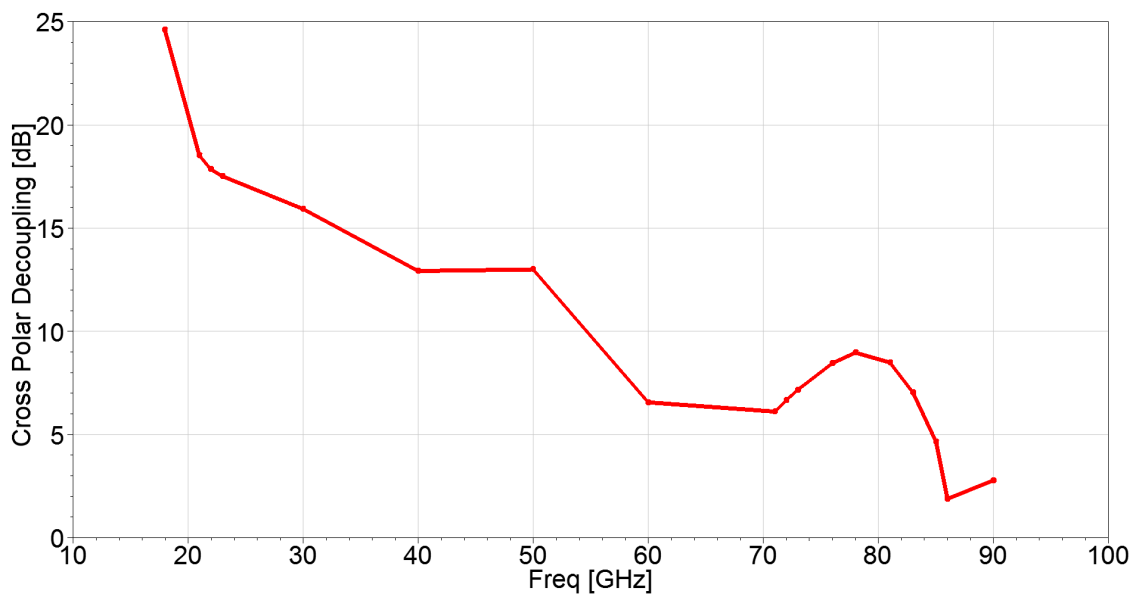


Figure 3.10: Cross-polarization Decoupling (XPD) in dB versus frequency when the *HOR* port is excited, for broadside radiation (8-by-8 elements of the infinite array are excited).

In a single polarization receiver antenna the cross-polarization level is the power of the orthogonal to excitation wave that can be received from the antenna. In a dual polarization situation there are elements in the orthogonal polarization so this power can be received from the antenna through them. In addition, the rotation of the E-field vectors will give higher XPD.

Fig. 3.10 reveals that when a signal with *HOR* polarization is transmitted it reaches the receiver antenna rotated in the azimuth, and a significant portion of it is entering the *VER* port. However, this is not an indication for the performance of a dual polarization antenna, as when both *HOR* and *VER* signals are transmitted they arrive in the receiver with high orthogonality, which is the desirable outcome. In addition, the placement of the receiver array antenna rotated around the boresight direction in respect to the transmitter array antenna, will help the separation of the orthogonal signals during the reception.

From polarization parallelity the polarization orthogonality can be calculated using the formula:

$$\Pi_{dB} = 10 \log_{10}(1 - \rho) \quad (3.3)$$

It is useful to plot polarization orthogonality and XPD in the same figure (see Fig. 3.11) in order to have a better overview for each frequency.

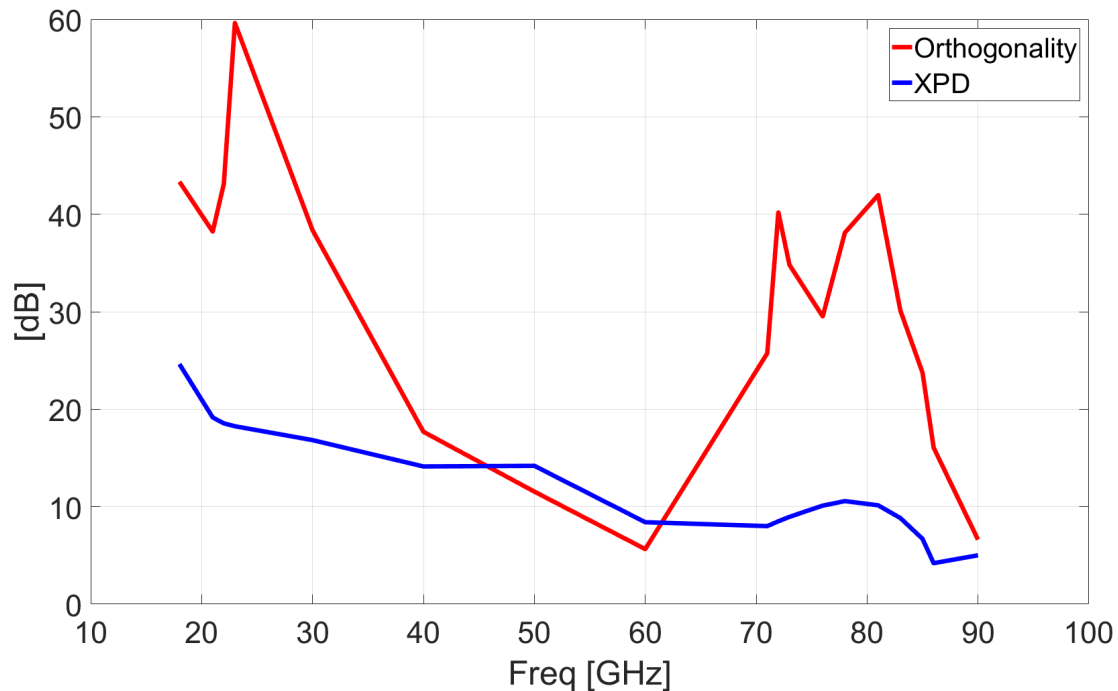


Figure 3.11: XPD and Polarization Orthogonality in dB versus frequency for broadside radiation (8-by-8 elements of the infinite array are excited).

3.2.3 Radiation Patterns

In Fig. 3.12 the normalized 2D radiation pattern at 22 GHz for broadside radiation can be seen. For the simulations in HFSS, 8-by-8 elements of the infinite array are excited in order to see how the radiation lobes formed in a large array.

In addition, in Fig. 3.13 and 3.14 the normalized radiation patterns at 73 GHz and 83 GHz are shown, using the same configuration. The absence of grating lobes in broadside direction is an outcome that was expected from the theory.

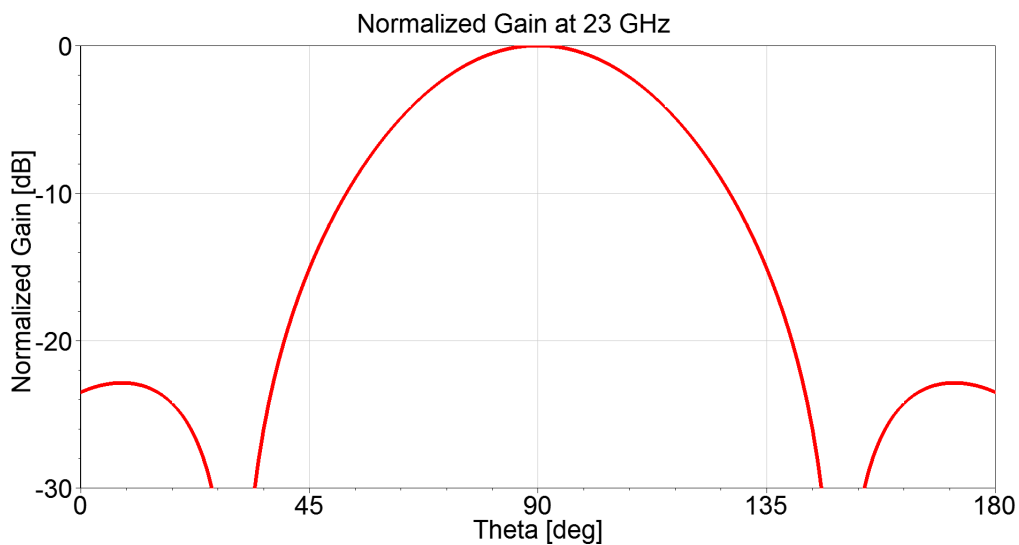


Figure 3.12: Normalized 2D radiation pattern at 23 GHz when 8-by-8 elements of the infinite array are excited in HFSS software.

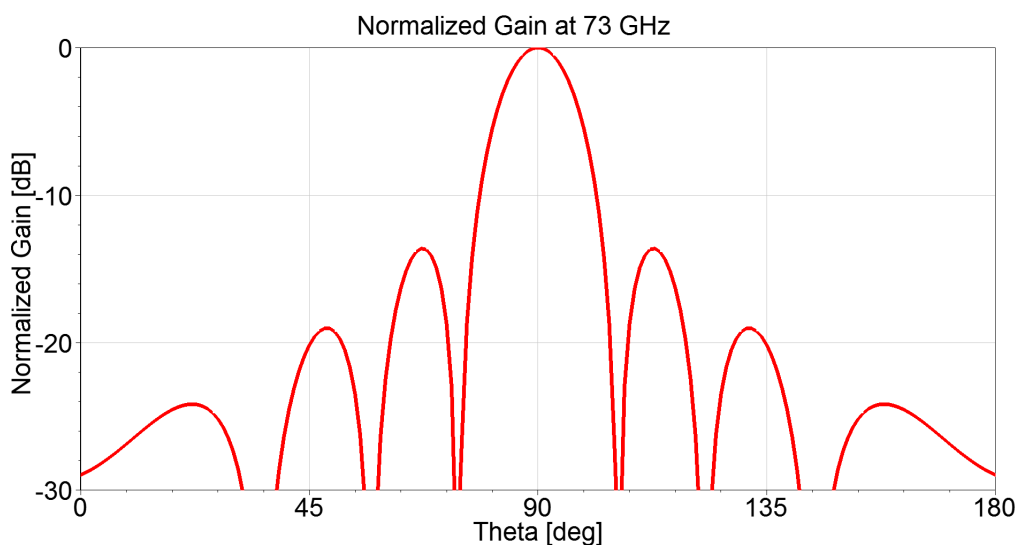


Figure 3.13: Normalized 2D radiation pattern at 73 GHz when 8-by-8 elements of the infinite array are excited in HFSS software.

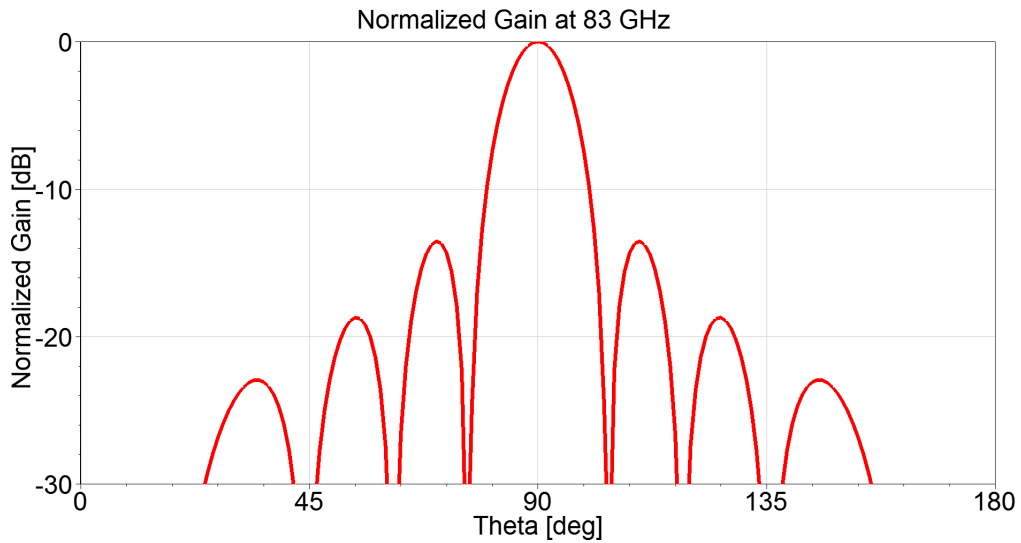


Figure 3.14: Normalized 2D radiation pattern at 83 GHz when 8-by-8 elements of the infinite array are excited in HFSS software.

3.3 Beam Steering

In this section the capability of the array to steer the beam is tested. It is reminded that the array antenna is designed for PtP fixed beam applications. It is useful to test the beam steering performance around broadside in small angles as it can be a useful feature for automatic fine antenna alignment.

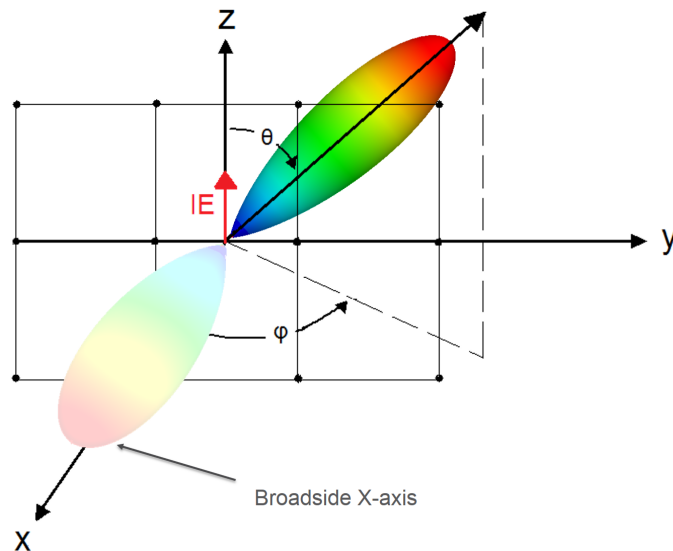


Figure 3.15: Planar array located in zy -plane with broadside radiation at \hat{x} direction. E-field vector's direction is the one used for the simulations when VER port is excited.

3. Design Analysis and Simulated Results

Assuming a scenario where the elements of the array are placed in the zy -plane, the broadside radiation is at $\hat{\mathbf{x}}$ direction ($\theta = 90^\circ$ and $\phi = 0^\circ$), as seen in Fig. 3.15. Furthermore, the VER ports are excited and the E-field vector has $\hat{\mathbf{z}}$ direction.

In order to test the beam steering along \mathbf{z} -axis (\mathbf{y} -axis), the phase of the excitation of the VER (HOR) elements should vary linearly, whereas the amplitude is kept uniform. For the simulations in HFSS the unit cell for an infinite array was used, where a phase delay was assigned in the periodic boundaries.

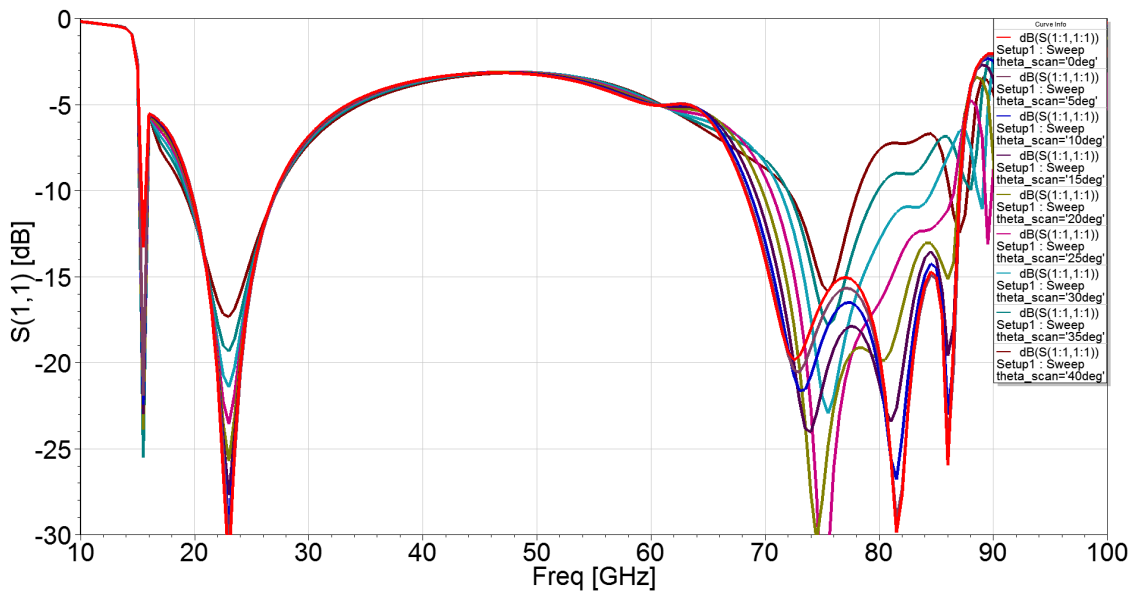


Figure 3.16: Return loss for beam steering in the xz -plane of the infinite array in HFSS software.

For beam steering along \mathbf{z} -axis a parameter $theta_scan$ is introduced that takes values for 0 to 40 degrees. In Fig. 3.16 the return loss for $theta_scan$ variations of θ around the broadside direction ($\theta = 90^\circ$ and $\phi = 0^\circ$) can be seen. In addition, in Fig. 3.17 the radiation patterns at 22 GHz and at 83 GHz for those scan angles can be seen.

The array antenna can successfully steer its beam 25 degrees at xz -plane for $\phi = 0^\circ$, which is more than enough for fine antenna alignment. Moreover, it shows great potential in beam steering capability, as it manages to steer the beam even though it has not been designed for that purpose.

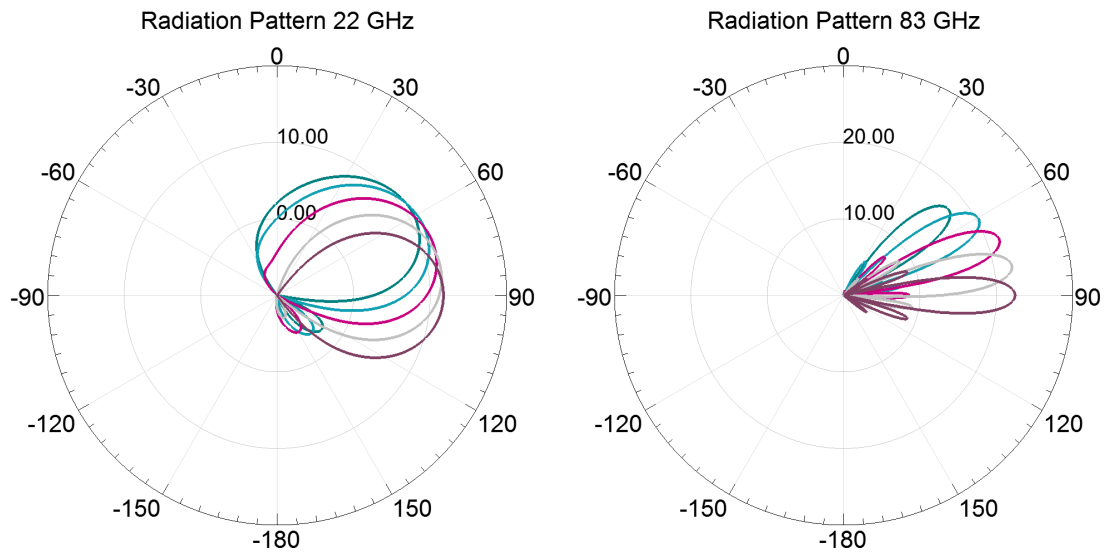


Figure 3.17: Realized gain at 22 GHz and 83 GHz for different beam θ angles and $\phi = 0^\circ$ (in the xz -plane) when 8-by-8 elements of the infinite array are excited in HFSS software.

For beam steering along y -axis a parameter phi_scan is introduced that takes values for 0 to 40 degrees. In Fig. 3.18 the return loss for phi_scan variations of ϕ around the broadside direction ($\theta = 90^\circ$ and $\phi = 0^\circ$) can be seen. In addition, in Fig. 3.19 the radiation patterns at 22 GHz and at 83 GHz for those scan angles can be seen.

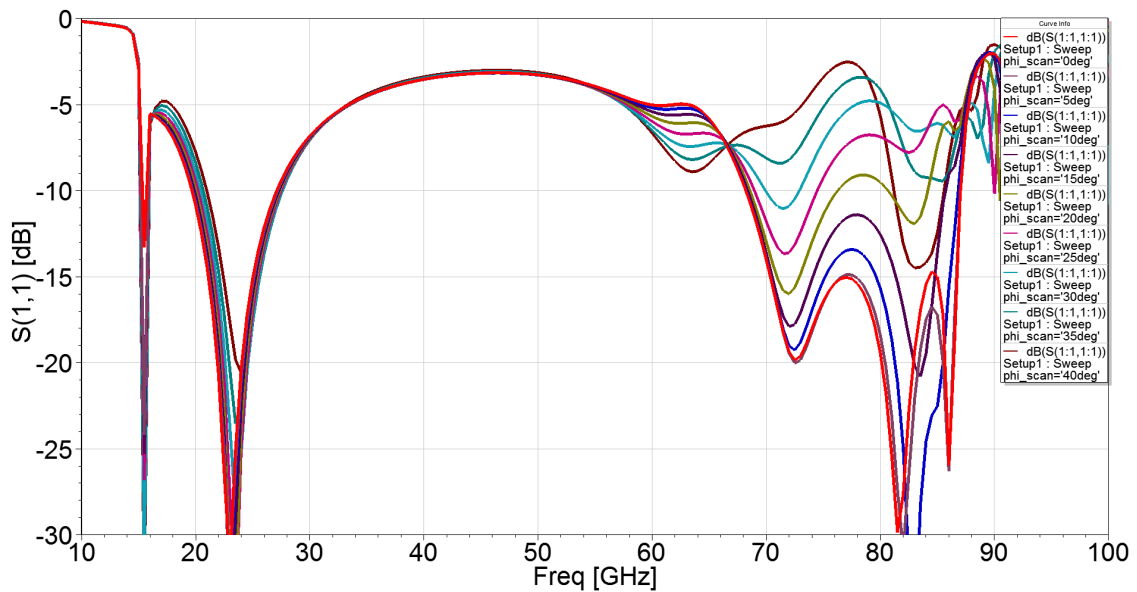


Figure 3.18: Return loss for beam steering in the xy -plane of the infinite array in HFSS software.

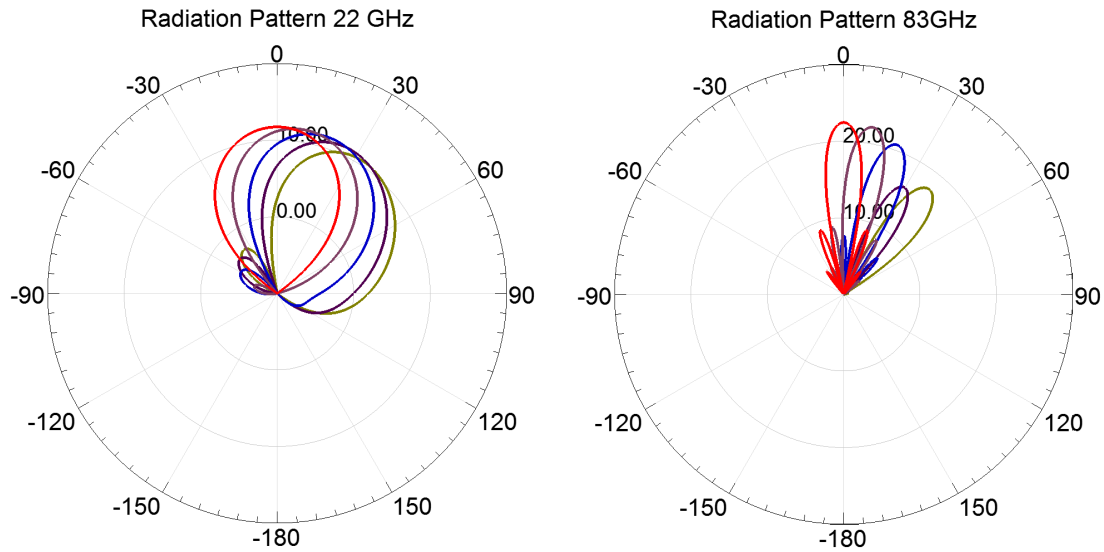


Figure 3.19: Realized gain at 22 GHz and 83 GHz for different beam ϕ angles and $\theta = 90^\circ$ (in the xy -plane) when 8-by-8 elements of the infinite array are excited in HFSS software.

The array antenna can successfully steer its beam 15 degrees at xy -plane for $\theta = 90^\circ$, which is enough for fine antenna alignment. We notice that the beam steering performance in this direction is not so good as at along z -axis for $\phi = 0^\circ$.

3.4 Tolerance Analysis

In this section a tolerance analysis of the structure has been performed. The tolerance analysis is performed using sensitivity analysis function of HFSS where parameters vary and a specific performance parameter is measured. Then, from that variance a curve is created and depending its slope one can see how sensitive is the structure performance to those variations.

Dimension tolerance analysis can be helpful during fabrication process in order to know which parameters should be focus and avoid mistakes. In the following figures there are the results of the analysis for three different frequencies having return loss (reflection coefficient) as a performance parameter. Each parameter varies around 20% around the optimal value.

3.4.1 Dimension Tolerance Analysis

First, a tolerance analysis of the dimensions of the structure carried out. From Fig. 3.20 it can be seen that the thickness of the copper does not affect the return loss at 22 GHz, whereas it is sensitive in variation of the substrate thickness, with 3 dB

to almost 10 dB difference in return loss for 10% substrate thickness variation. The reason for this is that for different substrate thickness the impedance of the element is changing and this results in shifting of the lower operation band of the array towards higher frequencies.

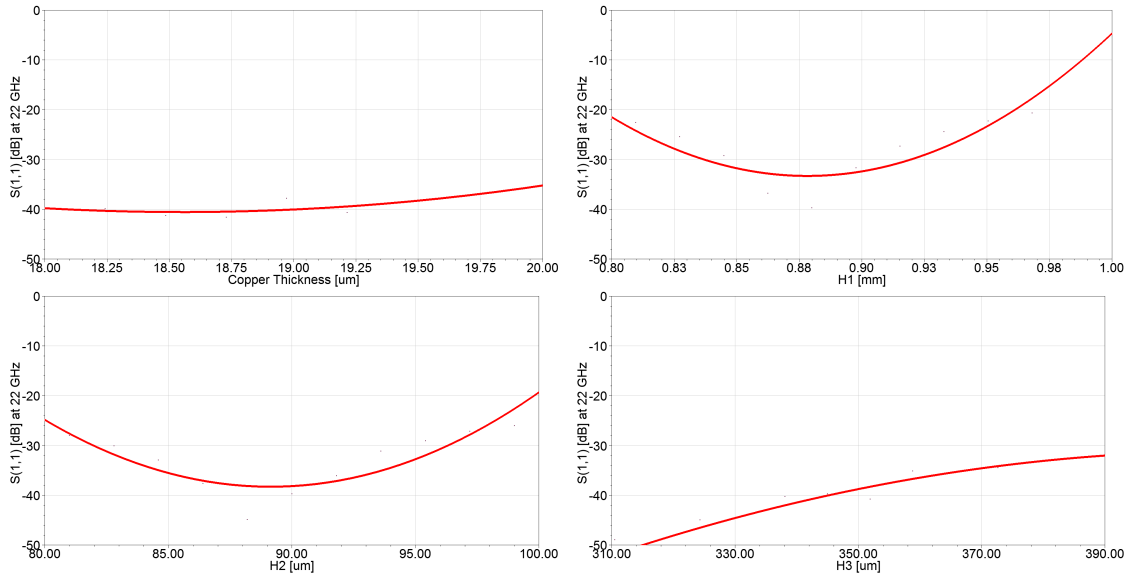


Figure 3.20: Structure’s reflection coefficient variation at 22 GHz for conductor and substrate thickness variation. Simulations made in HFSS.

Higher frequencies are also not sensitive in copper thickness variation, as it can be seen from Fig. 3.21 and Fig. 3.22. Moreover, the slope is larger for variation of substrate thickness, but not so large compared to 22 GHz.

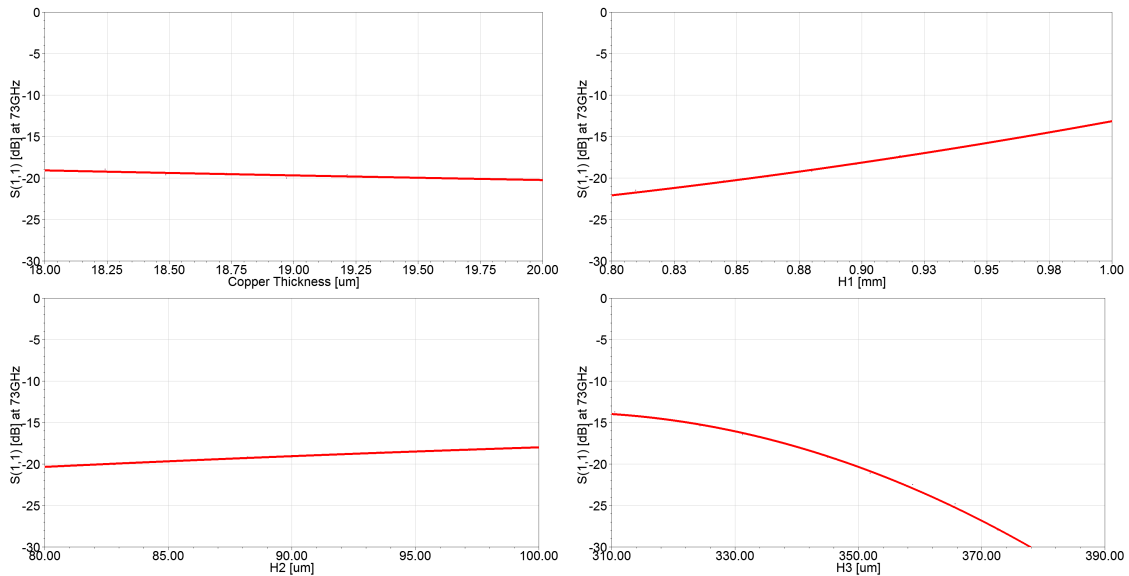


Figure 3.21: Structure’s reflection coefficient variation at 73 GHz for conductor and substrate thickness variation. Simulations made in HFSS.

3. Design Analysis and Simulated Results

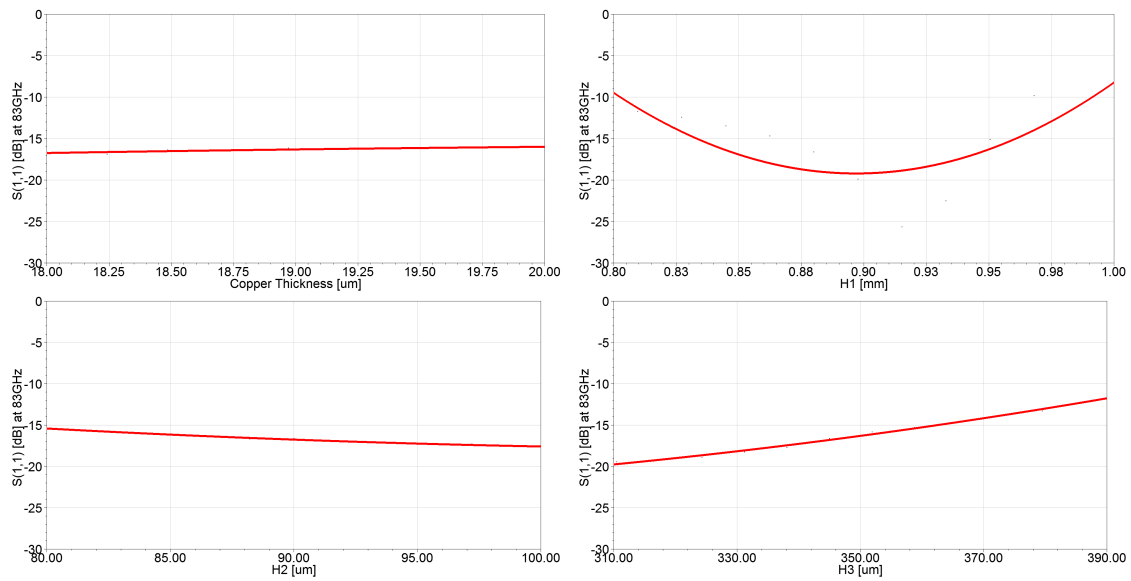


Figure 3.22: Structure's reflection coefficient variation at 83 GHz for conductor and substrate thickness variation. Simulations made in HFSS.

Figures 3.23, 3.24 and 3.25 contain the changes in return loss for different frequencies, when the parameters of the feeding network vary. Minor changes of those parameters result in significant changes of the feeding output impedance, which can be calculated by Eq. 2.30. The latter changes affect the return loss in all frequencies in a non related way.

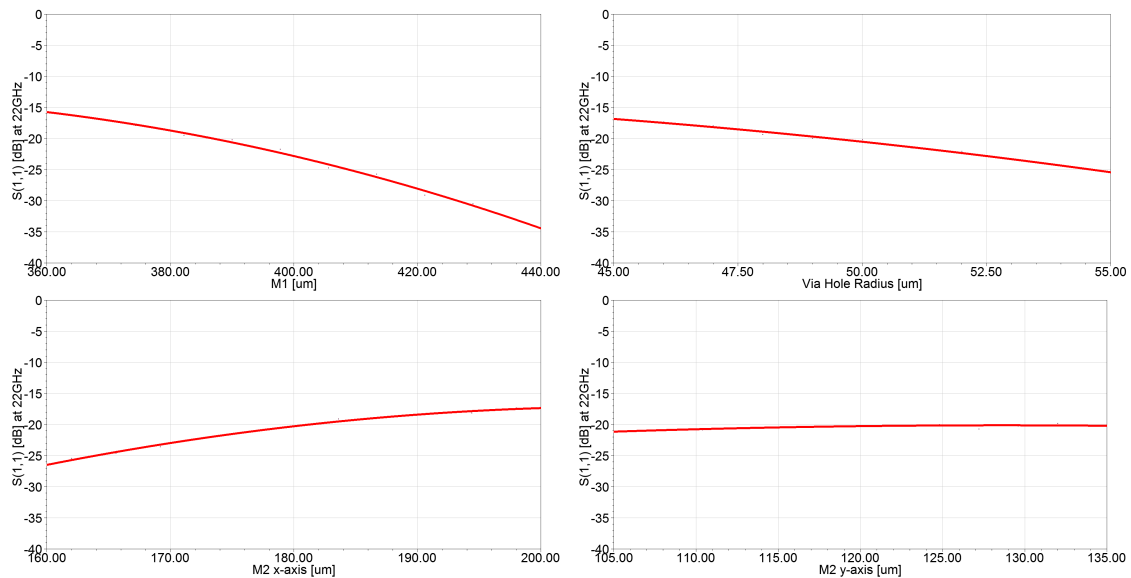


Figure 3.23: Structure's reflection coefficient variation at 22 GHz for feeding network dimensions variation. Simulations made in HFSS.

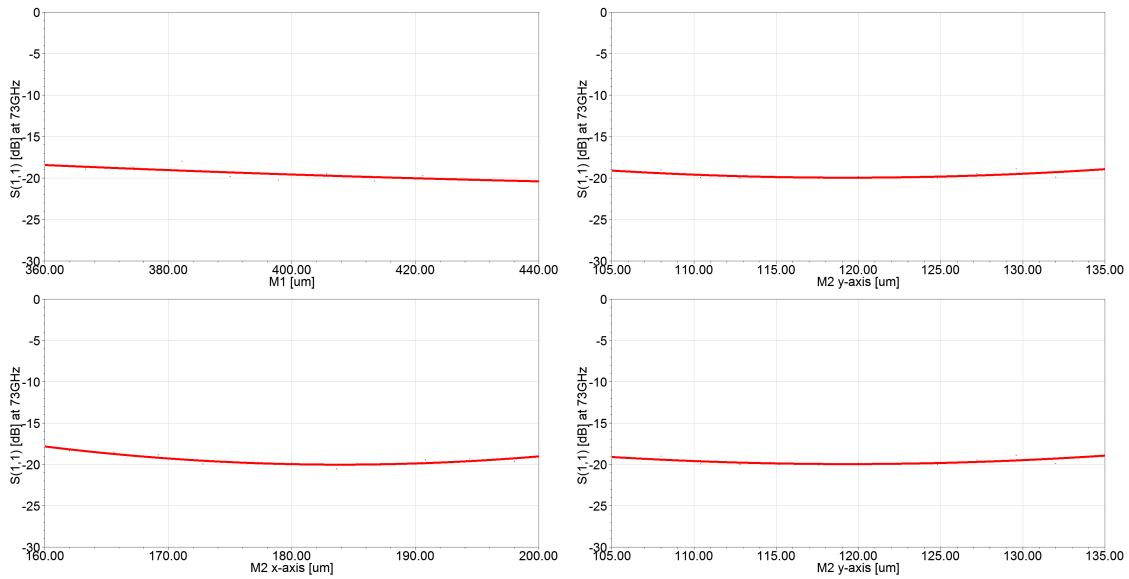


Figure 3.24: Structure’s reflection coefficient variation at 73 GHz for feeding network dimension variation. Simulations made in HFSS.

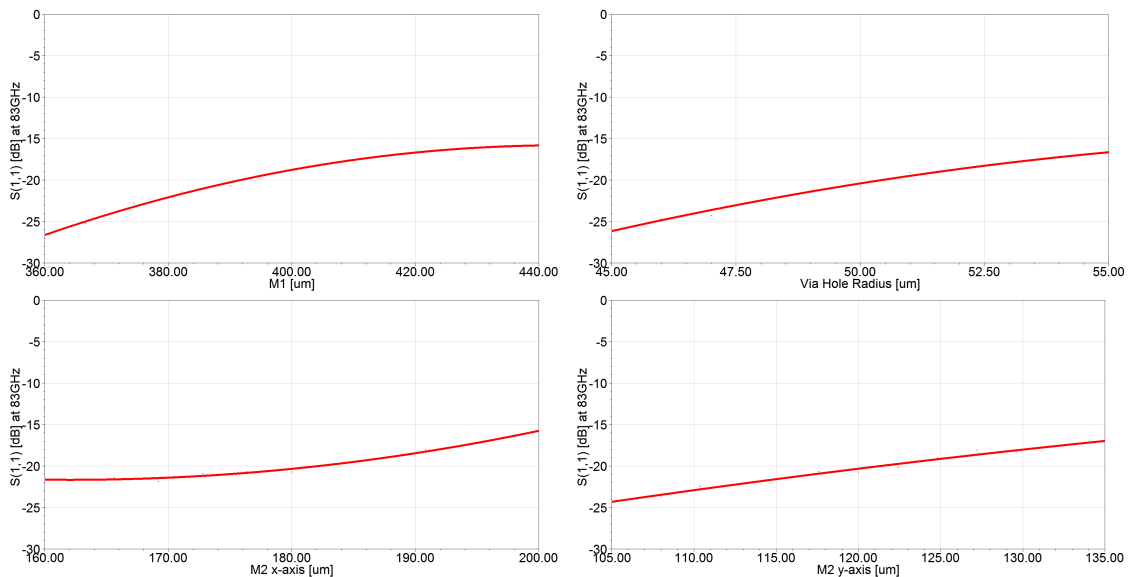


Figure 3.25: Structure’s reflection coefficient variation at 83 GHz for feeding network dimensions variation. Simulations made in HFSS.

In figures 3.26, 3.27 and 3.28 the reflection coefficient variation due to the element and the cap dimensions variations are shown.

The most affected frequency is the 22 GHz, where both the size of the element and the size of the caps shift the frequency. The second more sensitive frequency is the 83 GHz as the 73 GHz seems to be affected only by the size of the cap on top of the element. As it has been mentioned earlier, E-band and 23 GHz band are at the "limit" of the frequency range that the tightly coupled capped bow-tie array

3. Design Analysis and Simulated Results

operates. As a result, the lower frequencies of the 23 GHz band and the higher frequencies of the E-band are affected more by the variations of the dimensions of the structure.

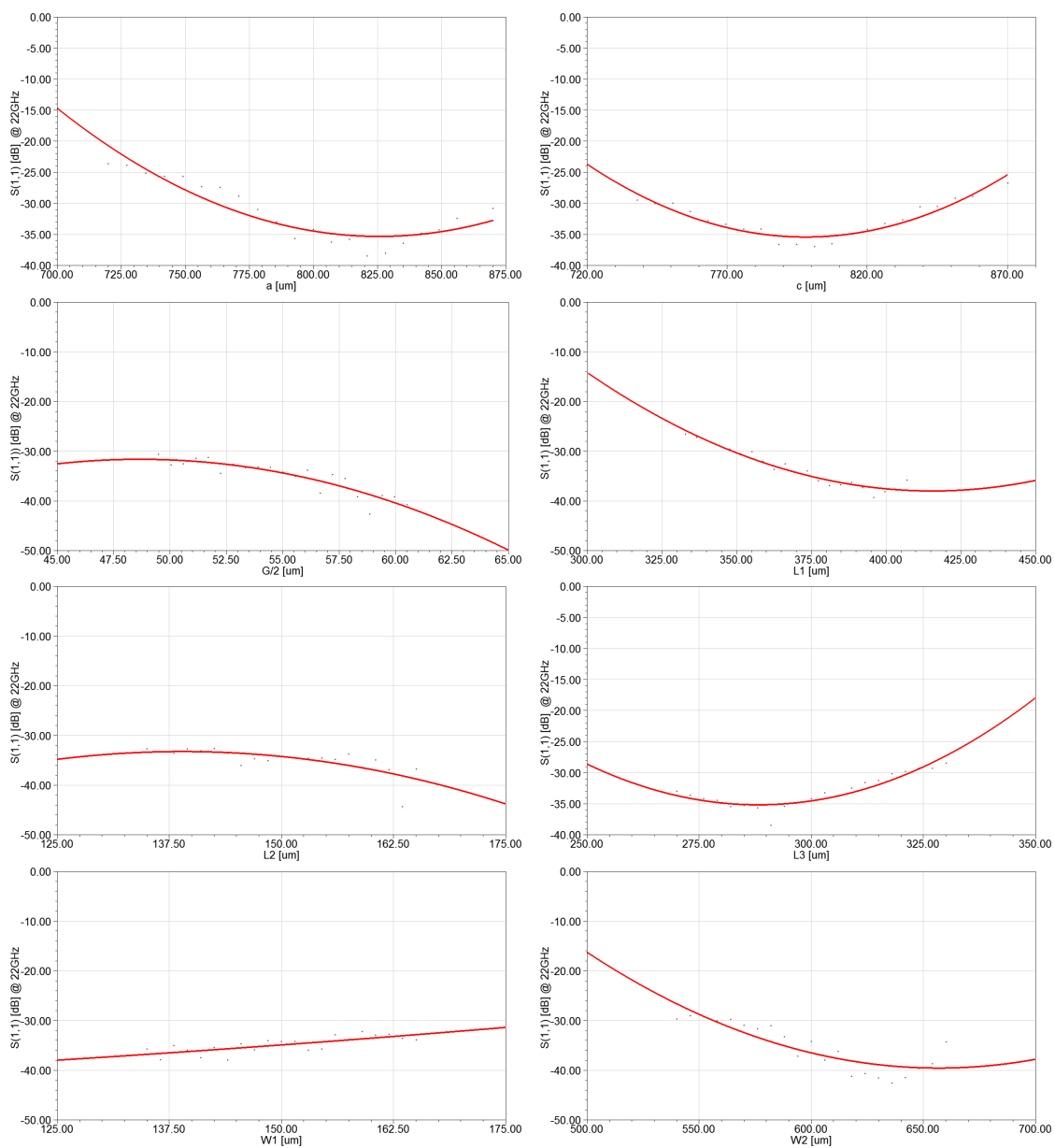


Figure 3.26: Structure's reflection coefficient variation at 22 GHz for element and cap dimensions variation. Simulations made in HFSS.

3. Design Analysis and Simulated Results

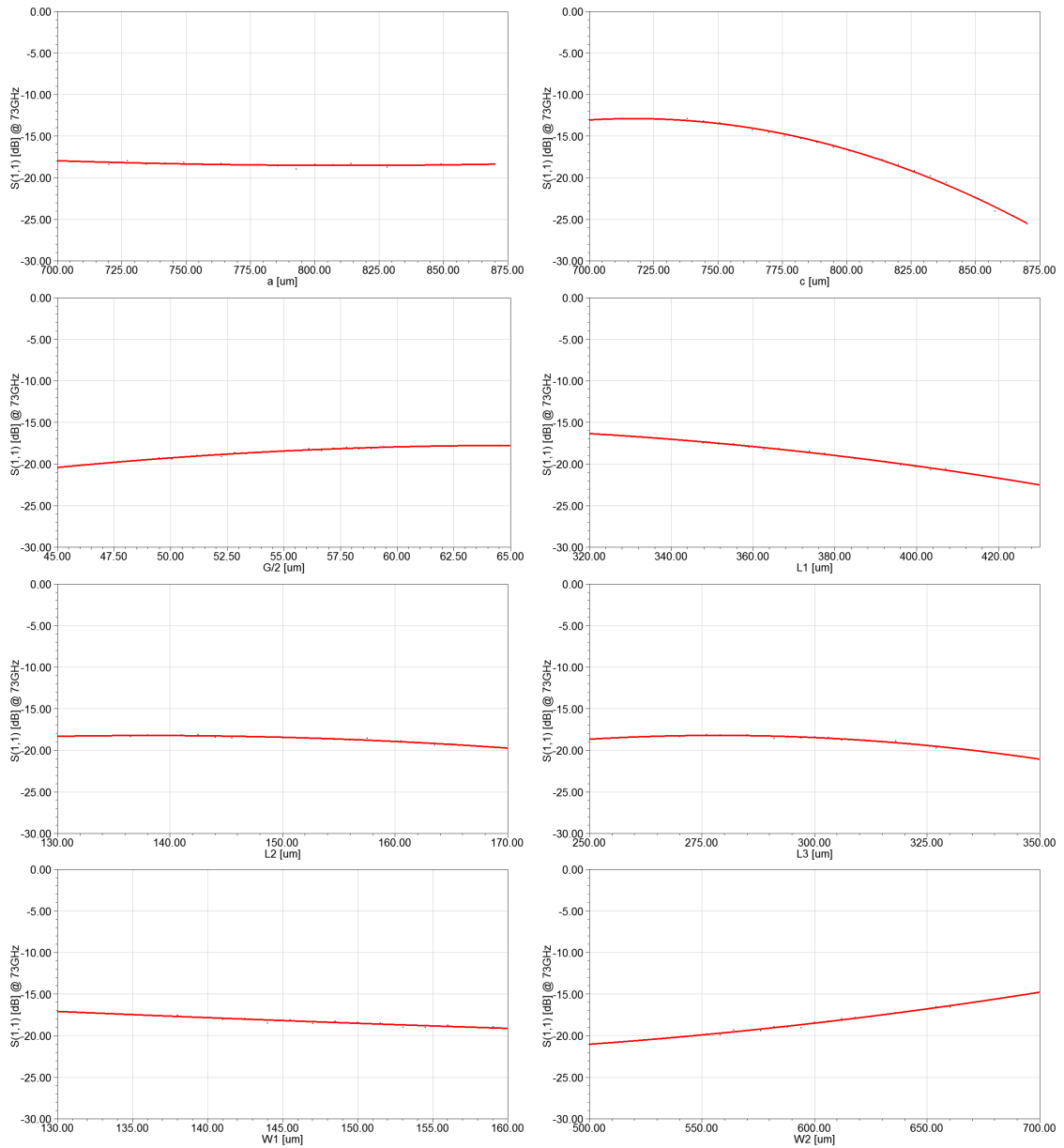


Figure 3.27: Structure's reflection coefficient variation at 73 GHz for element dimensions variation. Simulations made in HFSS.

3. Design Analysis and Simulated Results

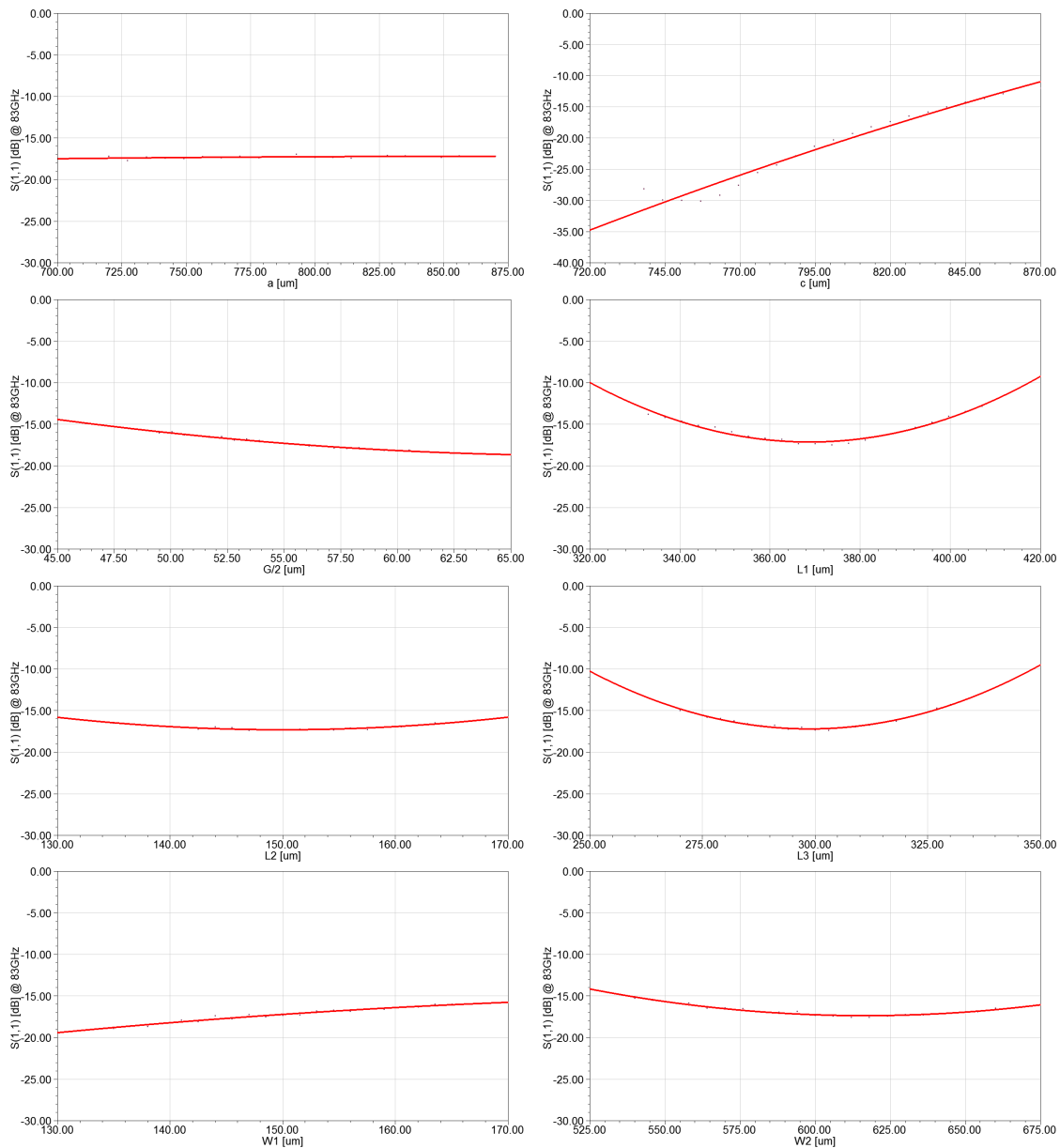


Figure 3.28: Structure's reflection coefficient variation at 83 GHz for element dimensions variation. Simulations made in HFSS.

3.4.2 Material Tolerance Analysis

In this section the material tolerance analysis of the dielectric substrates carried out. In Figures 3.29, 3.30 and 3.31 we can see the reflection coefficient variation when the core and the bonding material permittivity changes at 22 GHz, 73 GHz and 83 GHz respectively. The structure has high tolerance to 10% variation of the materials permittivity, as the reflection coefficient divergence is less than 1.5 dB.

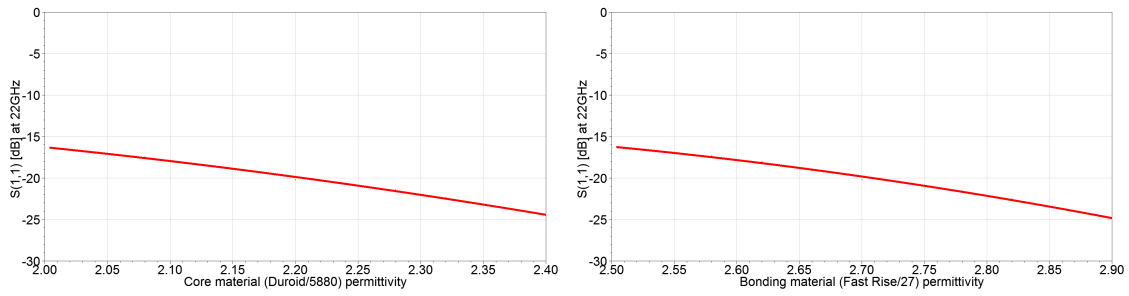


Figure 3.29: Structure's reflection coefficient variation at 22 GHz for material permittivity variation. Simulations made in HFSS.

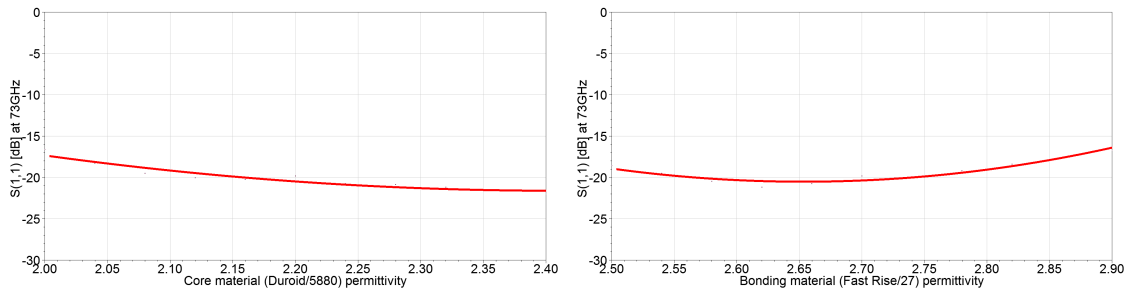


Figure 3.30: Structure's reflection coefficient variation at 73 GHz for material permittivity variation. Simulations made in HFSS.

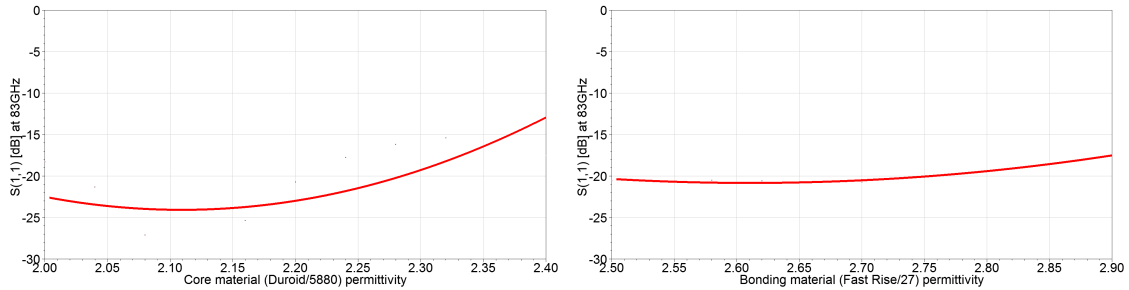


Figure 3.31: Structure's reflection coefficient variation at 83 GHz for material permittivity variation. Simulations made in HFSS.

4

Measurement and Fabrication Considerations

In this chapter there is a proposal for a 2-by-1 sub-array prototype to validate the capped bow-tie array, by fabrication and measurement of the return loss and the isolation. The sub-array can be placed upside down in a probe station with an absorbing material in the side of the radiation. In order to feed the elements an extra layer of bonding material TU-933P will be added in the bottom of the ground plane including a transition from probe pad (ground-signal-ground or GSG) to the feeding via hole. Some extra elements that do not have an input signal are also included in the design in order to avoid some edge effects. The final prototype design can be seen in Fig. 4.1.

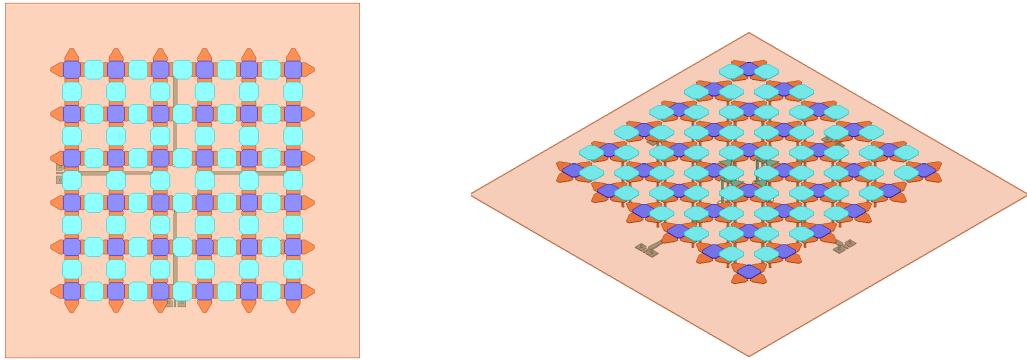


Figure 4.1: 2-by-1 dual polarization capped bow-tie sub-array prototype design.

The size condition that allows a planar array to radiate in a frequency band is that the aperture size should be at approximately 5λ -by- 5λ , where the wavelength is measured for the lowest frequency [23]. For this case the lowest frequency of operation is 21.1 GHz which gives an aperture $71.5 \times 71.5 \text{ mm}^2$. With an element spacing $S = 1.894 \text{ mm}$ (see Table 3.2) the minimum number of excited elements for radiation at 23 GHz band is 38-by-38. Therefore the aperture area of the prototype is not large enough to allow radiation at 23 GHz band and the number of elements is not large enough for tightly coupled array. However, this will provide a first low cost indication that the design resembles to reality so as we could move to larger

more costly arrays safely. The whole structure (the sub-array and the transition) will be simulated and the results will be compared to the measured ones. Good results are not expected, what matters is the resemblance between simulation and measurement.

Unfortunately, the fabrication procedure takes a lot of time and as a result the comparison between simulation and measurement will not be included in this work, but in a future one.

4.1 Transition from Element to Probe Pad

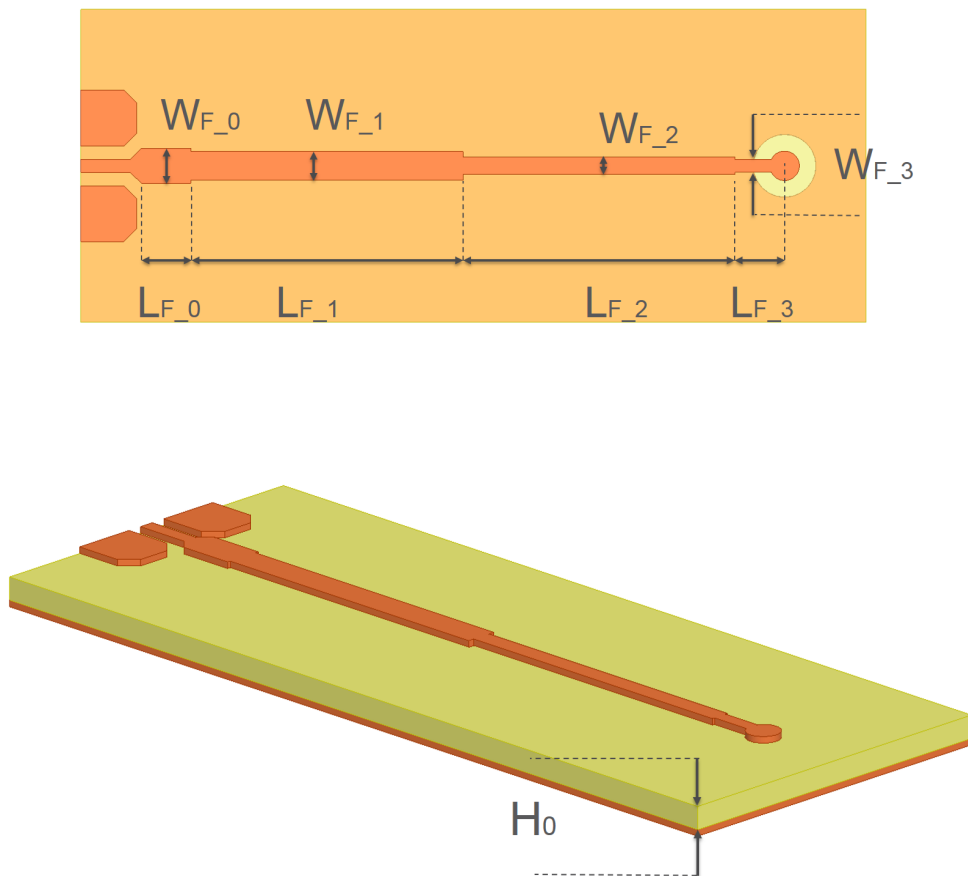


Figure 4.2: Transition from probe pad to element feeding via hole.

The transition from probe pad to element feeding via hole can be seen in Fig. 4.2. The first part from the left is a GSG pad with $100 \text{ } \mu\text{m}$ trace clearance, where the probe excites the structure. The two ground pads are connected through via

holes with the ground plane of the sub-array. As a bonding material TU-933P is used with $H_0 = 120 \text{ } \mu\text{m}$. A tapered transformer follows that is connected to a 50 ohm transmission line. The probe will be calibrated to this point to have 50 ohm impedance. After that there are two quarter wave transformers till a 77 ohm line, which is the input impedance of the balun transformer.

From microstrip transmission line theory [35] the widths of the lines are calculated using as:

$$\frac{W}{H} = \begin{cases} \frac{8e^A}{e^{2A} - 2} & \text{for } W/H < 1 \\ \frac{2}{\pi} \left[B - 1 - \ln(2B - 1) + \frac{\epsilon_r - 1}{2\epsilon_r} \left(\ln(B - 1) + 0.39 - \frac{0.61}{\epsilon_r} \right) \right] & \text{for } W/H > 1 \end{cases} \quad (4.1)$$

where

$$A = \frac{Z_0}{60} \sqrt{\frac{\epsilon_r + 1}{2}} + \frac{\epsilon_r - 1}{\epsilon_r + 1} \left(0.23 + \frac{0.11}{\epsilon_r} \right) \quad (4.2)$$

$$B = \frac{377\pi}{2Z_0\sqrt{\epsilon_r}}$$

The calculated values that are used in simulations are summarized in Table 4.1. Moreover the performance of the structure is seen in Fig. 4.3, the input wave port is de-embedded to the 50 ohm line and re-normalized to 50 ohm.

Table 4.1: Optimized design parameter values for transition from probe pad to element feeding via hole.

Parameter	(mm)	Parameter	(mm)
W_{F_0}	0.212	L_{F_0}	0.3
W_{F_1}	0.173	L_{F_1}	1.65
W_{F_2}	0.11	L_{F_2}	1.65
W_{F_3}	0.086	L_{F_3}	0.3

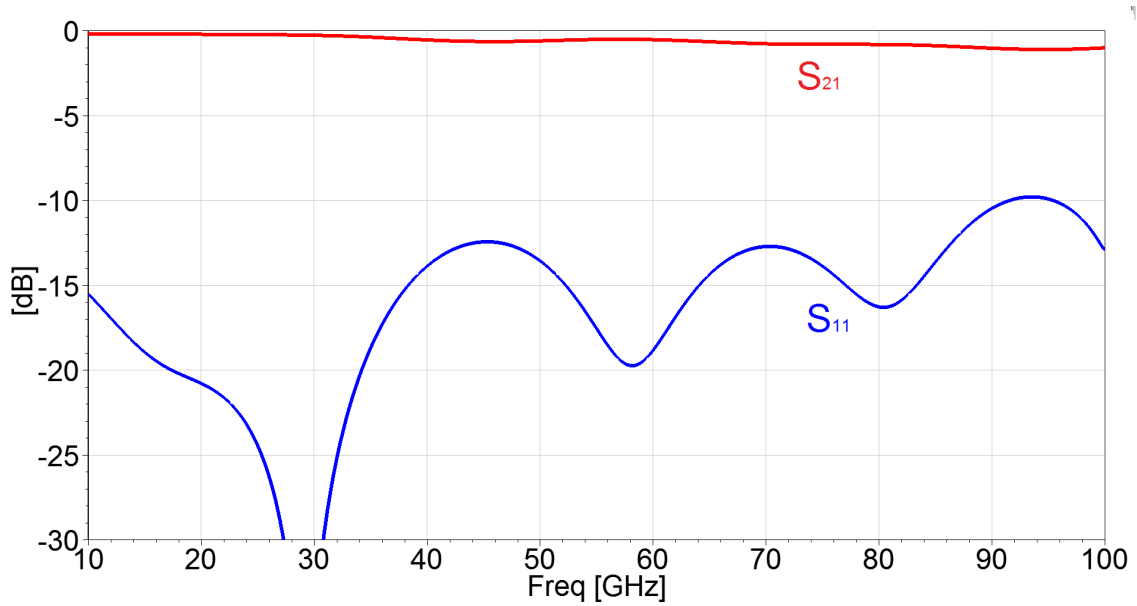


Figure 4.3: Transmission and reflection coefficients of the transition structure seen in Fig. 4.2.

4.2 Prototype Simulated Results

In this section the simulations of the prototype of the Fig. 4.1 carried out. A sub-array of 6-by-7 dual polarization capped bow-tie elements in multi-layer PCB is designed. All the elements have via holes to the ground plane, except from the edge elements. The 2-by-1 sub-array is connected to four baluns (two for each polarization), and the baluns are connected to the transitions seen in Fig. 4.2. Only the horizontal ports are excited (namely port 1 and port 2 for the simulations).

In Fig. 4.4 the return loss of port 1 and port 2 (the excited ports) can be seen. It is reminded that those results are expected to be worse compared to the return loss in Fig. 3.5, as the number of the total elements and the number of the excited elements are very small for TCA performance.

We can compare the return loss in port 1 if the sub-array consists of 3-by-4 elements, while again 2-by-1 are excited (see Fig. 4.5). The performance has even more declined, due to the smaller number of elements, despite the fact that in both cases 2-by-1 elements are excited.

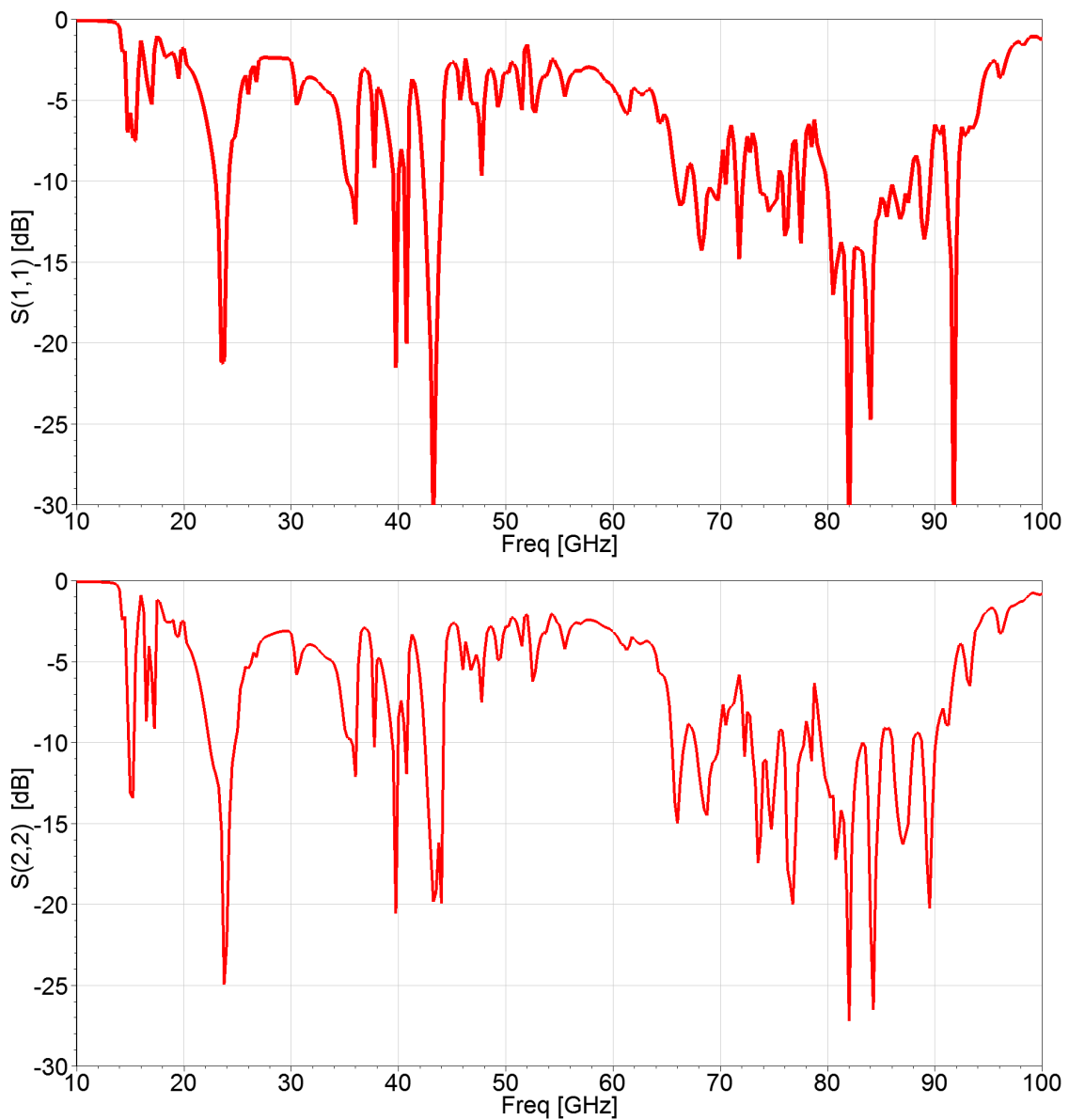


Figure 4.4: Return Loss of the two excited horizontal ports. A sub-array of 6-by-7 dual polarization capped bow-tie elements, where only 2-by-1 elements are excited.

The return loss is poor compared to the return loss of a large array with all the elements excited, as in Fig. 3.5, especially for the lower band, which confirms that a large number of elements needed in order to have large enough aperture area and TCA performance.

In Fig. 4.6 the mutual coupling between the two horizontal ports can be seen. For large array mutual coupling between ports of the same polarization is expected to be high.

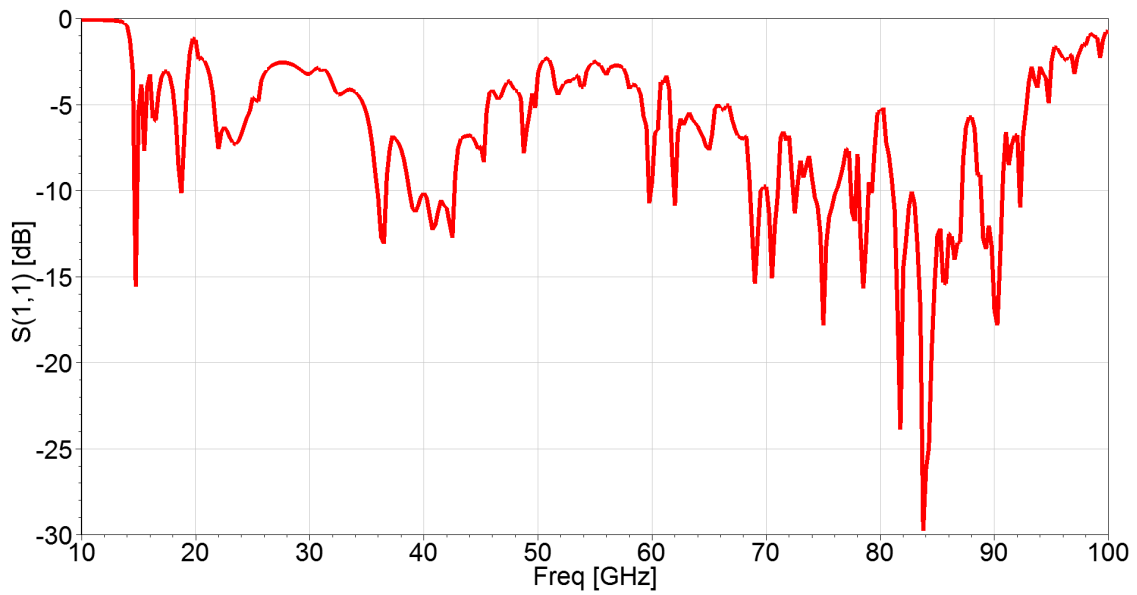


Figure 4.5: Return Loss of the two excited horizontal ports. A sub-array of 3-by-4 dual polarization capped bow-tie elements, where only 2-by-1 elements are excited.

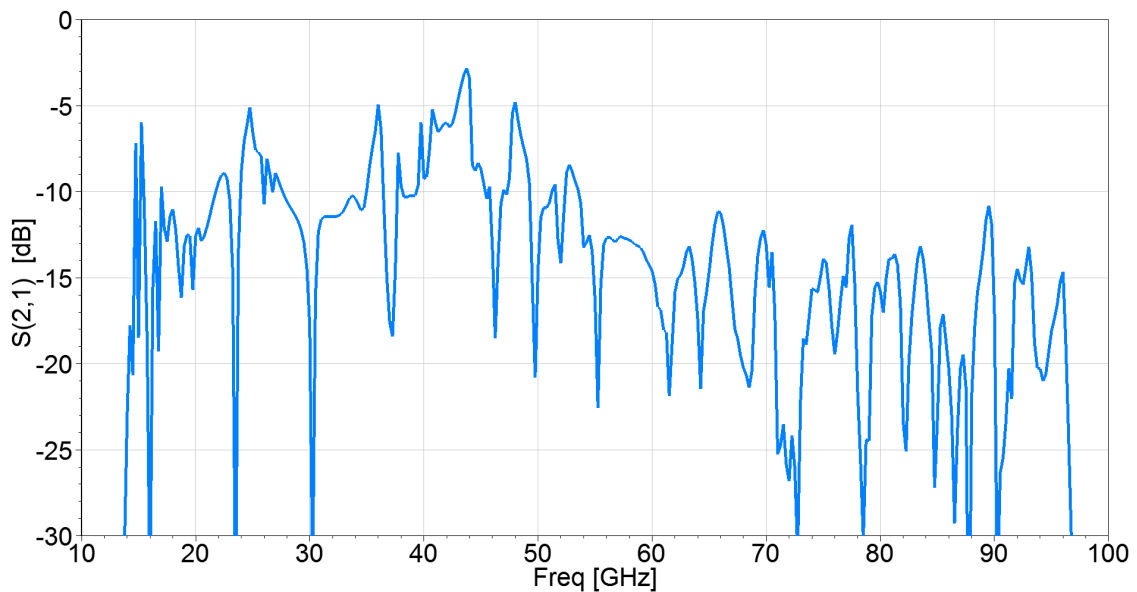


Figure 4.6: Mutual coupling between horizontal ports. A sub-array of 6-by-7 dual polarization capped bow-tie elements, where only 2-by-1 elements are excited.

Finally, in Fig. 4.7 the mutual coupling between the first horizontal port and the two vertical non-excited ports can be seen. We notice that the $S(4,1)$ in dB is significantly high for the 23 GHz band (corresponds to low isolation), as the aperture size is small from this band for radiation and as a result the power goes to port 4 and part of it returns to port 1 ($S(1,1)$ in dB is high for 23 GHz band).

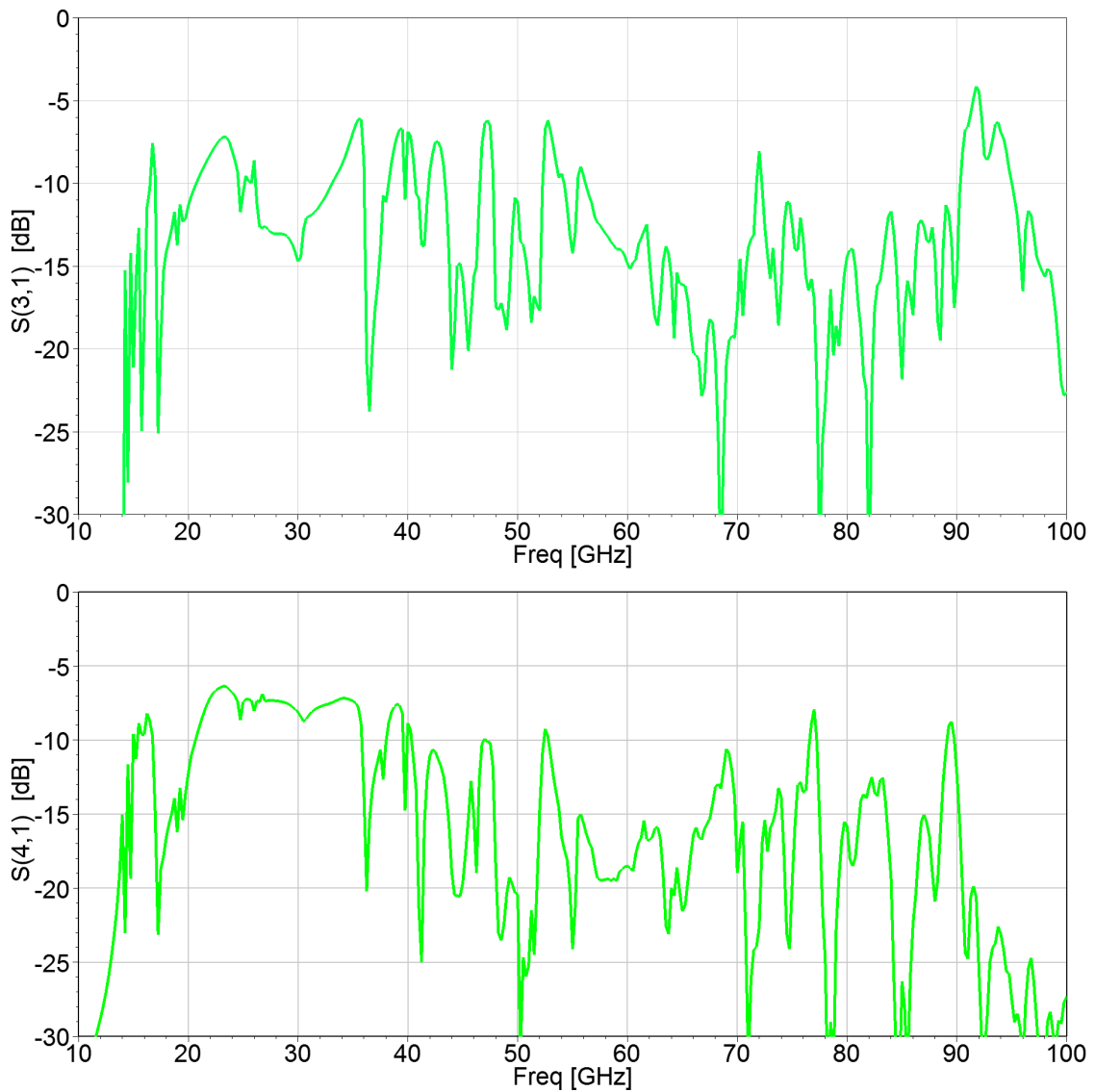


Figure 4.7: Mutual coupling between the first horizontal port and the two vertical non-excited ports. A sub-array of 6-by-7 dual polarization capped bow-tie elements, where only 2-by-1 elements are excited.

5

Conclusion

5.1 General Conclusions

In this work the design of a planar array in multi-layer PCB technology with capped bow-tie dual polarization elements operating at E-band and at 23 GHz band is presented. The simulations made with HFSS software, reveal that when the capped bow-tie element is implemented as a large TCA can provide more than 15 dB return loss at the two bands of interest, and at the same time keeps the orthogonality between the two linear polarizations in a level the fulfills the specification (except of two single frequencies but with potential to fulfill as well). Moreover, the array is capable of steering its beam 25 degrees around broadside in the plane parallel to E-field and 15 degrees around broadside in the plane tangent to E-field, which is satisfying for fine antenna alignment. On the other hand, the level of isolation between orthogonal ports should be higher. One, but still expensive solution is the use of a shielded feeding network.

In terms of dimension tolerance, the performance of the design can be easily declined and the lower operation band can be shifted, as more than 2 dB difference in return loss is observed with 10% changes in element/feeding dimensions and substrate thickness. The reason for that is the high dependence of the differential input impedance with the size of the element and the balun. On the other hand, the structure has high tolerance in changes of the materials permittivity.

Furthermore, the design shows high scalability potential, the size of the element, the size of the caps and the impedance provided by the feeding network can be tuned for operation at different frequency bands. It must be noticed that the frequency range limit expressed in fractional bandwidth is 4.2:1, so the two operating bands should be inside this fractional bandwidth.

In order to achieve an array gain more than 38 dBi at E-band, which consists a specification for PtP antennas, several thousands of elements are needed, and the complexity of the feeding network as well as the mechanics of the array will determine the total manufacturing cost.

When compared to access point antennas in street level or in residential and public

areas this solution is more promising, as gain specification is more relaxed requiring less elements and less complex feeding structure. Furthermore, the operating frequencies are lower, so making elements and element spacing larger results in lower fabrication cost and higher inter-port isolation (feeding via hole distance is larger).

In addition, a prototype is designed and simulated in order to be fabricated and measured. Simulations revealed that the performance in terms of return loss is degraded compared to a large array, as the number of elements is not sufficient for TCA operation and radiation at 23 GHz band. However, the resemblance between the simulations and the measurements can be a first indication to validate the design and proceed to larger arrays fabrication.

5.2 Future Work Proposal

This work only includes a proposal for a prototype and the validation of it requires its fabrication and measurement. For this reason a future work that will focus on the this matter should be done.

In addition, it would be interesting to test the dual polarization capped bow-tie TCA antenna design for access point array antennas and also test the beam steering capability.

Finally, a more detailed work for the feeding network that includes the total losses should be done. Different structures for differential feeding network should be investigated, in order to improve the isolation between orthogonal ports and the losses.

Bibliography

- [1] J. Yang, P.-S. Kildal, "FDTD design of a chinese hat feed for shallow mm-wave reflector antennas," IEEE AP-S International Symposium, Atlanta, June, 1998.
- [2] M. Denstedt, T. Ostling, J. Yang, P.-S. Kildal, "Tripling bandwidth of hat feed by genetic algorithm optimization," IEEE AP-S 2007 in Hawaii, 10-15 June 2007.
- [3] W. Wei, J. Yang, T. Ostling, T. Schafer, "New hat feed for reflector antennas realized without dielectrics for reducing manufacturing cost and improving reflection coefficient," IET Microwaves Antennas & Propagation 5 (2011) 837-843.
- [4] E. G. Geterud, J. Yang, T. Ostling, P. Bergmark, "Design and optimization of compact wideband hat-fed reflector antenna for satellite communications," IEEE Transactions on Antennas and Propagation 61, 125-133, 2013.
- [5] E. G. Geterud, J. Yang, T. Ostling, "Wide band hat-fed reflector antenna for satellite communications," in Proceedings of the 5th European Conference on Antennas and Propagation, EUCAP 2011. Rome, 11-15 April 2011, pp. 754-757.
- [6] E. G. Geterud, J. Yang, T. Ostling, "Radome design for hat-fed reflector antenna," in Proceedings of 6th European Conference on Antennas and Propagation, EuCAP 2012. Prague, 26-30 March 2012, pp. 2985-2988.
- [7] J. Yang, A. Kishk, "A novel low-profile compact directional ultra-wideband antenna: the self-grounded bow-tie antenna," IEEE Transactions on Antennas and Propagation 60 (2012) 1214-1220.
- [8] Y. Yu, J. Yang, T. McKelvey, B. Stoew, "Compact UWB indoor and through-wall radar with precise ranging and tracking," International Journal of Antennas and Propagation 2012 (2012) Article ID 678590.
- [9] H. Raza, A. Hussain, J. Yang, P.-S. Kildal, "Wideband compact 4-port dual polarized self-grounded bowtie antenna," IEEE Transactions on Antennas and Propagation 62 (2014) 4468-4473.
- [10] J. Yang, A. Kishk, "The self-grounded bow-tie antenna," in 2011 IEEE International Symposium on Antennas and Propagation, Spokane, USA, 3-8 July,

- 2011, 2011, pp. 1452-1455.
- [11] S. Abtahi, J. Yang, S. Kidborg, "A new compact multiband antenna for stroke diagnosis system over 0.5-3 GHz," *Microwave and Optical Technology Letters* 54 (2012), 2342-2346.
 - [12] Jian Yang, Jonas Flygare, B. Billade, "Development of quadruple-ridge flared horn with spline-defined profile for band b of the wide band single pixel feed (WBSPF) advanced instrumentation programme for SKA," in *2016 IEEE AP-S International Symposium*, Puerto Rico, June 25-July 1, 2016, 2016.
 - [13] B. Munk et al., "A Low-Profile Broadband Phased Array Antenna," *Antennas and Propagation Society International Symposium*, 2003. *IEEE* , vol.2, no., pp. 448- 451 vol.2, 22-27, June 2003.
 - [14] Justin A. Kasemodel, Chi-Chih Chen, and John L. Volakis, "A Miniaturization Technique for Wideband Tightly Coupled Phased Arrays," *Antennas and Propagation Society International Symposium*, 2009. *APSURSI '09. IEEE* , vol., no., pp.1-4, 1-5, June 2009.
 - [15] Chin-Shen Lin et al., "Analysis of Multiconductor Coupled-Line Marchand Baluns for Miniature MMIC Design," *IEEE Transactions On Microwave Theory And Techniques*, vol. 55, no. 6, June 2007.
 - [16] Steven S. Holland, and Marinos N. Vouvakis, "The Planar Ultrawideband Modular Antenna (PUMA)," *IEEE Transactions on Antennas and Propagation*, vol. 60, no. 1, January 2012.
 - [17] Markus H. Novak, Felix A. Miranday, and John L. Volakis, "An Ultra-Wideband Millimeter-Wave Phased Array," in *European Conference on Antennas and Propagation (EuCAP)*, 2016 .
 - [18] Markus H. Novak, Felix A. Miranday, and John L. Volakis, "Low Cost Ultra-Wideband Millimeter-Wave Array," *IEEE International Symposium on Antennas and Propagation (APSURSI)*, 2016 .
 - [19] William F. Moulder, Kubilay Sertel, and John L. Volakis, "Ultrawideband Superstrate-Enhanced Substrate-Loaded Array With Integrated Feed," *IEEE Transactions on Antennas and Propagation*, vol. 61, no. 1, November 2013.
 - [20] William F. Moulder, Kubilay Sertel, and John L. Volakis, "Superstrate-Enhanced Ultrawideband Tightly Coupled Array With Resistive FSS," *IEEE Transactions on Antennas and Propagation*, vol. 60, no. 9, September 2013.
 - [21] Mark Jones, and James Rawnick, "A New Approach to Broadband Array Design Using Tightly Coupled Elements," *Harris Corporation*, Melbourne, FL, 2007.

-
- [22] D. Bartholomew, "Optimum design for a broadband microstrip balun," *Electronics Letters*, vol. 13, no. 17, pp. 510–511, August 1977.
- [23] Henrik Holter and Hans Steyskal, "Some Experiences From FDTD Analysis of Infinite and Finite Multi-Octave Phased Arrays," *IEEE Transactions on Antennas and Propagation*, vol. 50, no. 12, December 2002.
- [24] Timothy E. Durham et al., "Design of an 8-40 GHz Antenna for the Wideband Instrument for Snow Measurements," *IEEE International Symposium on Antennas and Propagation & USNC/URSI National Radio Science Meeting*, July 2015.
- [25] D. S. Filipovic et al., "Modeling, Design, Fabrication, and Performance of Rectangular μ -Coaxial Lines and Components," *IEEE MTT-S International Microwave Symposium Digest*, June 2006.
- [26] William F. Moulder, "Novel Implementations of Ultrawideband Tightly Coupled Antenna Arrays," Ph.D dissertation, The Ohio State University, 2012.
- [27] Justin A. Kasemodel, "Realization of a Planar Low-Profile Broadband Phased Array Antenna," Presented in Partial Fulfillment of the Requirements for the Degree Doctor of Philosophy, The Ohio State University, 2010.
- [28] Nathanael J. Smith, "Development of a 180⁰ Hybrid Balun to Feed a Tightly Coupled Dipole X-Band Array," Senior Honors Thesis, The Ohio State University, 2010.
- [29] Kalyany Vinayagamoorthy, "Design and Implementation of Wideband Baluns for Archimedean Spiral Antennas," Master's Thesis, Queensland University of Technology, August 2011.
- [30] Jonas Edstam, "Microwave Backhaul Gets a Boost with Multiband," *Ericsson Technology Review, Charting the Future of Innovation*, vol. 93, January 2016.
- [31] John L. Volakis, "Ultra Wideband Phased Arrays and Transceivers," *IEEE International Symposium on Antennas and Propagation, Workshop 5*, October 2006.
- [32] Mikael Coldrey et al., "Wireless Backhaul in Future Heterogeneous Networks," *Ericsson Review*, pp. 28-36, February 2014.
- [33] Kildal, Per-Simon. *Foundations of Antenna Engineering: A Unified Approach for Line-of-Sight and Multipath*. Gothenburg: Kildal Antenna AB, 2015. Print.
- [34] Mailloux, Robert J.. *Phased Array Antenna Handbook*. Boston: Artech house, Inc, 1994. Print.
- [35] Pozar, David M.. *Microwave Engineering*, 4th Edition. Massachusetts: John Wiley & Sons, Inc, 2012. Print.

- [36] ETSI GS mWT (V1.1.1): “millimetre Wave Transmission (mWT); Analysis of antennas for millimetre wave transmission”.
- [37] ETSI EN 300 833 (V1.4.1): “Fixed Radio Systems; Point-to-point antennas; Antennas for point-to-point fixed radio systems; Antennas for point-to-point fixed radio systems operating in the frequency band 3 GHz to 60 GHz”.
- [38] ETSI EN 302 2177-4-2 (V1.5.1): “Fixed Radio Systems; Characteristics and requirements for point-to-point equipment and antennas; Part 4-2: Antennas; Harmonized EN covering the essential requirements of article 3.2 of the R&TTE Directive”.